Distribution Agreement

In presenting this thesis as a partial fulfillment of the requirements for a degree from Emory University, I hereby grant to Emory University and its agents the non-exclusive license to archive, make accessible, and display my thesis in whole or in part in all forms of media, now or hereafter now, including display on the World Wide Web. I understand that I may select some access restrictions as part of the online submission of this thesis. I retain all ownership rights to the copyright of the thesis. I also retain the right to use in future works (such as articles or books) all or part of this thesis.

Alan C. W. Rohrbach April 9, 2019

Swelling of Poly(methyl methacrylate) Films in Different Solvent Vapor Environments: A Comparison of Solvents Used in Nanolithographic Processing

by

Alan C. W. Rohrbach

Connie B. Roth
Adviser

Department of Physics

Connie B. Roth

Adviser

Eric R. Weeks

Committee Member

David Zureick-Brown

Committee Member

2019

Swelling of Poly(methyl methacrylate) Films in Different Solvent Vapor Environments: A Comparison of Solvents Used in Nanolithographic Processing

By

Alan C. W. Rohrbach

Connie B. Roth

Adviser

An abstract of
a thesis submitted to the Faculty of Emory College of Arts and Sciences
of Emory University in partial fulfillment
of the requirements of the degree of
Bachelor of Sciences with Honors

Department of Physics

2019

Abstract

Swelling of Poly(methyl methacrylate) Films in Different Solvent Vapor Environments: A Comparison of Solvents Used in Nanolithographic Processing

By Alan C. W. Rohrbach

Polymer films are used extensively as sacrificial resist layers in the nanolithographic process. Their properties as resists are quantified by sensitivity, the minimum dose required to expose the resist, and contrast, a measure of how quickly the resist goes from completely unexposed to completely exposed. Existing work in the lithographic field determines sensitivity and contrast of polymer resist layers through the production of contrast curves, which are functions of exposure dose. However, this method makes it hard to isolate the effects of developer solvent conditions from other variables. Solvent conditions are very important to nanolithography since the development step of the process depends on finding and maintaining a delicate balance of solvent quality to achieve selective dissolution. In positive-tone resists, the solvent used must selectively dissolve away the short chain segments in the regions exposed by the electron beam while leaving undisturbed the unexposed regions. This work looks at the interaction of a widely used polymer resist with the solvent/non-solvent pair that is most often used in its lithographic processing, without the confounding factors of electron beam exposure.

We designed and fabricated a sample chamber for use on an ellipsometer to allow samples of polymer films to be exposed to a solvent vapor environment while being measured by spectroscopic ellipsometry. The sample chamber consists of an aluminum base with a solvent "moat" surrounding the sample itself and a 3D printed polypropylene lid with a viewing window, solvent filler hole, and openings for the beam path. Initial measurements were made using the sample chamber and samples of poly(methyl methacrylate) (PMMA) exposed to either isopropyl alcohol (IPA) or methyl isobutyl ketone (MIBK) vapor. We observed faster swelling in the PMMA films exposed to MIBK vapor than in the PMMA films exposed to IPA vapor, which agrees with our expectation that MIBK will behave as a solvent and IPA as a non-solvent.

Swelling of Poly(methyl methacrylate) Films in Different Solvent Vapor Environments: A Comparison of Solvents Used in Nanolithographic Processing

By

Alan C. W. Rohrbach

Connie B. Roth

Adviser

A thesis submitted to the Faculty of Emory College of Arts and Sciences
of Emory University in partial fulfillment
of the requirements of the degree of
Bachelor of Sciences with Honors

Department of Physics

2019

Acknowledgements

I would like to thank Eric Weeks and David Zureick Brown for taking the time to be part of the committee. I would also like to thank all the members of the Roth laboratory, especially Louis Han and Jennifer McGuire. I extend my gratitude to all my friends and family, and especially to my mother, for their love and support.

I am deeply grateful to Horace Dale, Benjamin Kasavan, and Robin Horton for their assistance in the fabrication of my sample chamber.

Above all, I thank my adviser Connie Roth for her outstanding mentorship and vital role in the creation of this work.

Table of Contents

Table of Figures

Chapter 1. Introduction and Background

1.1 Introduction to Electron Beam Lithography

Nanolithography is a branch of nanotechnology concerned with the fabrication of nanometer-scale structures. The general principle of lithography is the use of a layer that resists certain processing steps that can be manipulated to create patterns to be transferred to other media. In the fabrication of semiconductor devices, further processing steps might include the deposition of additional material or the etching away of some material already present on the substrate.

In electron beam lithography (EBL), polymers such as poly(methyl methacrylate) (PMMA) are often used as a resist layer that is patterned by exposure to a beam of high-energy electrons. Exposure to the electron beam causes changes in the polymer that allow it to be selectively washed away. The pattern of where the resist is removed determines where additional material deposited onto the sample will stick to the substrate.

Electron beam lithography is widely used in the electronics industry as well as scientific research of nanoscale systems. Using electron beam lithography, it is possible to produce many interesting and useful features. For example, in the electronics industry, EBL is used to make the transistors and other circuit elements that constitute microprocessors and other semiconductor devices that are now ubiquitous. In physics research labs, EBL is used to produce samples that can be used to study phenomena that emerge at the nanoscale [1].

1.1.1 Process of EBL

Polymers are a popular choice as a resist layer for lithography because they can be spin-coated onto a substrate with minimal preparatory steps. Spin-coating is a process used to deposit

uniform thin films onto flat substrates by using centrifugal force to spread the coating material. Spin-coating is fast and creates a layer with a uniform thickness that can be precisely controlled by varying the spin speed and concentration of the solution [2]. Comprehensive curves of film thickness as a function of spin speed at various solution concentrations have already been created for some of the most popular combinations of polymer and solvent used in lithography. Spin coating also allows the reliable manufacture of thin films, down to thicknesses less than 10 nm [3].

The lithographic process can be understood as a series of steps, which are summarized in Figure 1. First, the substrate is cleaned, and the polymer resist layer is spin-coated onto the sample and heated to drive off residual solvent. Second, a pattern is exposed into the resist using an electron beam, either by a lithography tool or a scanning electron microscope. The electron beam causes the polymer to undergo chain scission, breaking it into small pieces. In the third step, these small pieces are washed away by a solvent called the developer. The developer must be a solvent that does not readily remove the unexposed resist, but does wash away the shorter chains left behind by chain scission. In the case of PMMA as a resist, two solvents are commonly used as developers: methyl isobutyl ketone (MIBK) and isopropanol (IPA). Next, the layers of metal that make up the nanostructure to be studied are deposited. Many different layers of metals may be deposited through sputtering. Finally, the excess metal deposited on top of the resist stack is removed through a process called “Lift-off.” In this process, the remaining portion of the resist layer is released from the substrate surface by a stronger solvent, and as this remaining polymer film washes away, any of the metal that is not attached directly to the substrate also comes off. When working with PMMA, the solvent used in this step is usually acetone. Finally, the sample is cleaned, dried, and then ready for study.

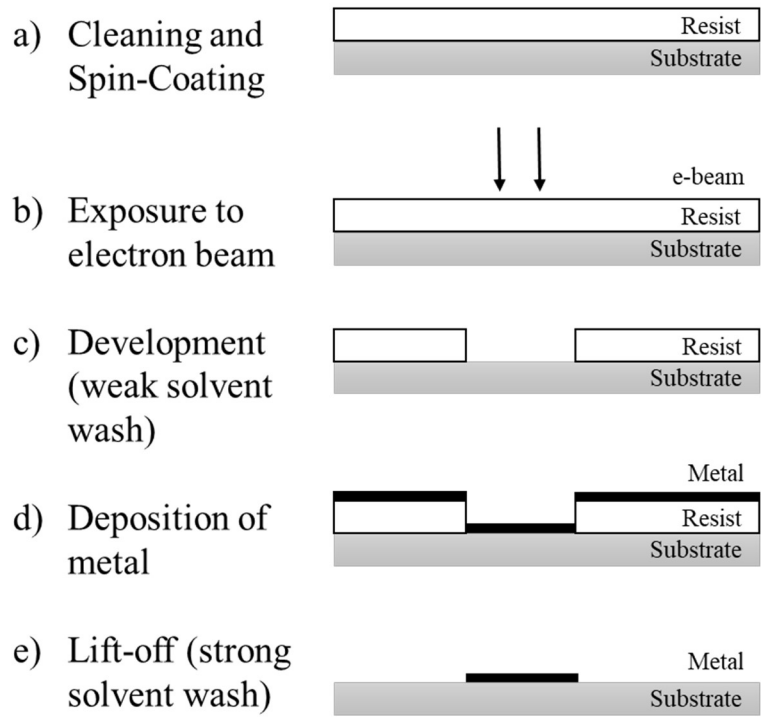

Figure 1. Simplified version of the electron beam lithographic process. Polymers (such as PMMA) are common as a resist layer, and silicon is a common substrate. The metal deposited onto the sample will often be composed of many layers of different metals and alloys. (a) Step 1: cleaning of the substrate and spin-coating of the polymer resist. Using PMMA as a resist, cleaning usually consists of an acetone bath. (b) Step 2: exposure to electron beam, causing chain scission in the polymer. (c) Step 3: development of the resist by exposure to a weak solvent like MIBK or IPA. (d) Step 4: deposition of uniform layers of metal, usually via sputtering or evaporation. (e) Step 5: lift-off. The remaining resist is removed by a wash in a stronger solvent, like acetone.

1.1.1.1 Positive and Negative Tone

The process described above applies for so-called positive tone lithography, where exposure to the electron beam causes chain scission, which makes the exposed area easier to wash away with a solvent. In a positive-tone resist, the pattern exposed into the resist is the same pattern that will be applied to the substrate during further processing. On the other hand, overexposure to the electron beam causes crosslinking, which has the opposite effect. The pattern is negated, and further processing will affect everywhere except the exposed area of the

resist. This is called a negative-tone resist. Figure 2 illustrates the difference between these two types of resists.

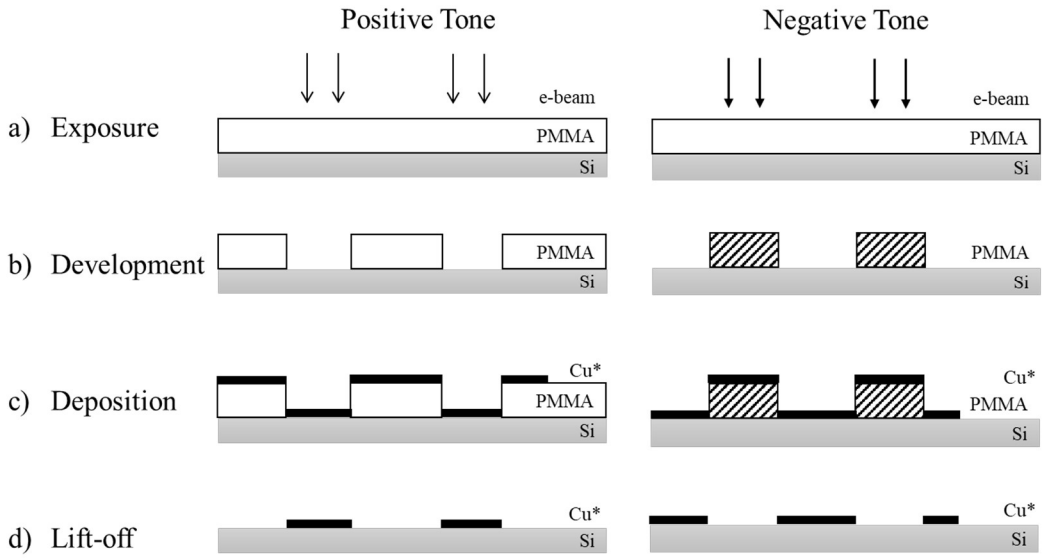

Figure 2. Comparison of process flow for positive-tone and negative-tone resists as used in electron beam lithography. (a) Negative-tone processing of PMMA uses a higher exposure dose than positive-tone processing does. (b) In the positive-tone process, weak solvents like MIBK and IPA are used for development. In the negative-tone process, acetone is used. (c) Deposition procedure is unchanged. (d) While positive-tone lift-off uses acetone, negative-tone lift-off requires O_2 plasma etching.

1.1.2 Sample Geometry

A certain sample geometry, called "undercut," is widely used to help improve the lift-off process [4]. A more sensitive copolymer resist is cast onto the substrate, and a less sensitive PMMA resist layer is cast on top of it. Since the copolymer is more sensitive to the e-beam, it will undergo a greater amount of chain scission, making it dissolve more quickly in the solvent used in the development process, creating a larger open space below the PMMA layer. This prevents the layer of metals deposited by sputtering from attaching itself up the sides of the polymer stack, and thus makes it easier to remove the unwanted metal. The result is a cleaner

deposited layer of metal to work with, with no so-called "wings" of metal that stick up at the edges. Figure 3 illustrates the difference between an undercut sample and a single layer sample.

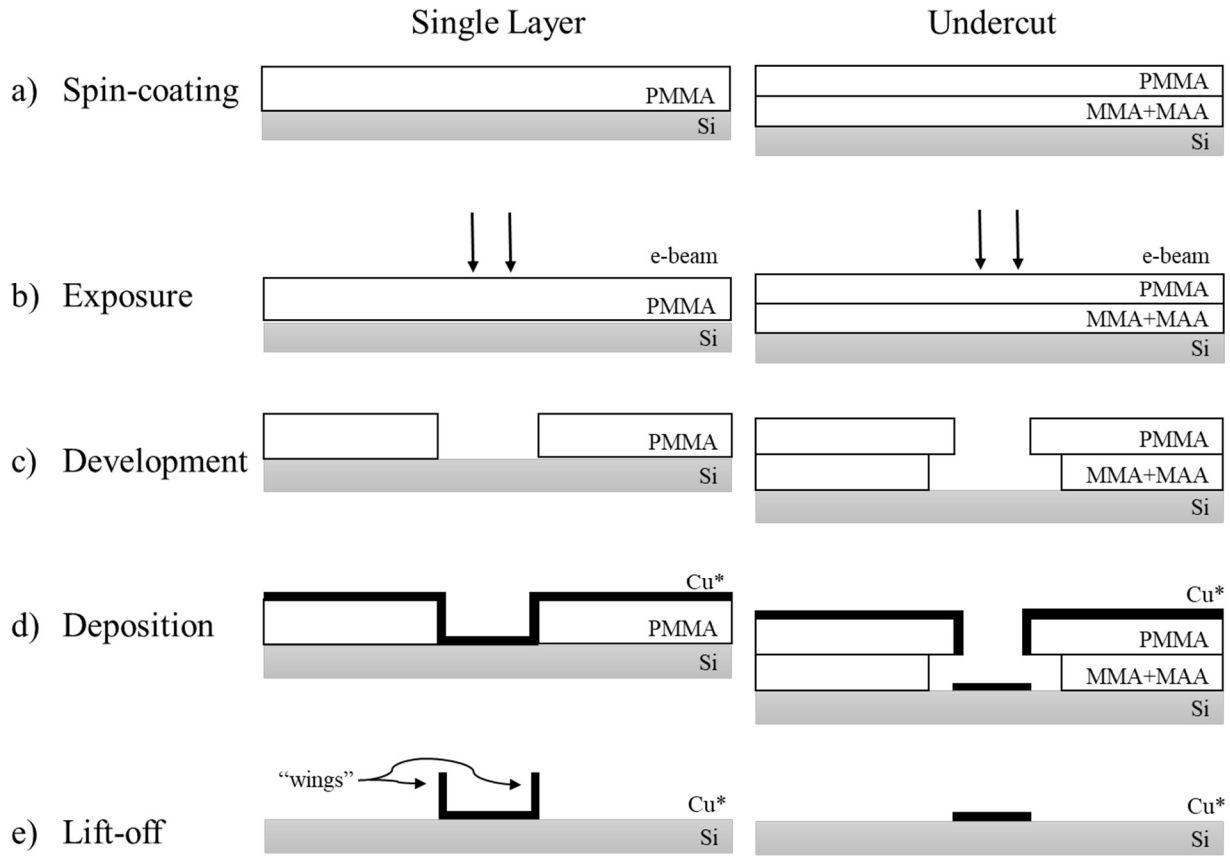

Figure 3. Comparison of process flow for a single layer sample geometry versus an undercut sample geometry. The undercut is preferable because it prevents the elevated "wings" of metal from sticking to the sample. (a) To create an undercut geometry, the PMMA resist layer is spin-coated on top of a more sensitive copolymer resist layer. (b) Exposure dose may have to be fine-tuned in the undercut case to account for different sensitivities. (c) Development results in the more sensitive copolymer layer dissolving in a larger area such that the upper layer of PMMA overhangs. (d) During deposition, especially via sputtering, a layer of metal may stick to the sides of the resist layers. The undercut geometry prevents this layer from becoming attached to the layer deposited on the substrate. (e) Lift-off is easier to achieve when the deposited metal is not attached to the resist layer, and there are no abnormal shapes left behind on the sample.

1.2 Relevant Properties of Polymers

Polymers are long molecules made of a chain of repeating monomer units connected covalently. Each chain of monomers is one polymer molecule, and these molecules can become

quite large, typically spanning several tens of nanometers. It can even be argued that an entire rubber band or car tire is one molecule because of the permanent covalent crosslinks between chains. When discussing the length of a polymer, *degree of polymerization* quantifies the number of monomers in the chain. It is also possible to express the size of polymer molecules in terms of their molecular weight. Since polymers are produced with a statistical distribution of chain lengths, there are multiple ways to determine the average molecular weight of a polymer. The first is the *number average molecular weight,* an ordinary arithmetic mean calculated as $M_n = \frac{\sum_i N_i M_i}{\sum_i N_i}$ [5]. The second is the *weight average molecular weight*, which is an average weighted by each chain's mass. It is calculated as $M_w = \frac{\sum_i N_i M_i^2}{\sum_i N_i M_i}$. The width of the distribution of chain lengths can be described by the polydispersity index, $\text{PDI} = \frac{M_w}{M_n}$ [5].

Another important property of polymers is the *glass transition temperature* T_g. T_g is a temperature defined on cooling when an equilibrium liquid becomes a non-equilibrium solid. As the material cools, it falls out of equilibrium and solidifies because it becomes kinetically trapped, without enough energy available to explore all of the substance's configurational possibilities [6]. T_g can be measured experimentally as the temperature on cooling at which the rate of thermal expansion changes. The glass transition has been studied in polymers because it represents a sudden, dramatic change in the dynamics of a material over the course of cooling by tens of degrees. For example, the modulus of polymers increase by three orders of magnitude at T_g when transitioning from the rubbery melt state to the glassy solid state (modulus increases from MPa to GPa) [6].

T_g is subject to interfacial effects. In particular, the presence of a free surface tends to increase local mobility and therefore decrease local T_g, while substrate interfaces can vary

between having little to no effect and having a very strong effect that decreases local mobility and therefore increases local T_g [7]. As samples are confined to thin films, the ratio of surface area to volume increases, and the effects at the interfaces start to compete with each other and dominate the dynamics of the entire film [7]. These interfacial effects can have important implications for nanofabrication as resist layers are made smaller and more complicated geometries further increase the surface area to volume ratio of the resists. However, this study will avoid these effects by studying only bulk polymer films (200 nm thick or thicker).

1.2.1 Polymer Solubility in Solvents

Flory-Huggins theory describes the mixing of polymers. The model starts from regular solution theory, which describes the increase in entropy upon mixing based on modeling a solution as a lattice of black and white balls. Flory-Huggins theory assumes that the lattice sites are the size of solvent molecules, and that therefore the larger polymer molecules occupy N lattice sites connected in a chain. Thus, N is the ratio of the polymer's molar volume to the solvent's molar volume, and is proportional to the polymer's degree of polymerization and therefore to its molecular weight [5].

The result of Flory-Huggins theory for a polymer solution is the following equation:

$$\frac{\Delta G_m}{kT} = \phi_1 \ln(\phi_1) + \frac{\phi_2}{N}\ln(\phi_2) + \phi_1\phi_2\chi, \quad (1)$$

where ΔG_m is the free energy gain upon mixing, $\phi_1 = \frac{m_1}{m_1+Nm_2}$ is the volume fraction of the solvent, $\phi_2 = \frac{Nm_2}{m_1+Nm_2}$ is the volume fraction of the polymer, and χ is an interaction parameter that describes the interaction energy of the polymer with the solvent [5]. The first two terms represent the contribution of entropy to the change in free energy, while the last term represents the enthalpy of mixing. Since the volume fractions ϕ are between 0 and 1, $\ln(\phi)$ is always

negative, indicating that entropy favors mixing [5]. Since N is in the denominator of the second term, it is clear that shorter chains will mix more easily than longer chains will. Finally, the χ parameter encapsulates the interactions between the solvent and the polymer. A solvent with too large of a χ will fail to dissolve the polymer, while a good solvent will have a small value for χ. A poor solvent falls somewhere in between the good solvent and nonsolvent cases, with an intermediate value of χ that allows it to dissolve a polymer only if it has sufficiently small chains. A final note is that since the free energy gain ΔG_m upon mixing is proportional to the temperature, polymers will tend to be more soluble at higher temperatures.

1.3 Electron Dose on Polymers and Contrast Curves

Exposure to the electron beam has effects on the properties of polymers used as resist layers. Low doses of electron-beam exposure cause chain scission, a process whereby bonds between adjacent monomers in the chain break, changing one long chain into two shorter chains. As the chains are cut up into shorter pieces, they become easier to dissolve and wash away. However, a very large dose of exposure to the electron beam can cause crosslinking, where monomer units make bonds between chains, essentially becoming a tightly bound disordered mess. Once a polymer becomes crosslinked, it is much more difficult to remove with solvent.

1.3.1 Contrast Curves

In terms of optimizing the lithographic process, it is complicated to determine how much a sample should be exposed to the electron beam in order to produce the desired results. Dose of exposure to the electron beam is measured in units of charge per area, usually microcoulombs per square centimeter. To determine how much exposure is required to completely remove the resist from the substrate during development (called the *clearing dose*), it is necessary to make a series of samples which all have the same thickness of resist layer and expose each of them to a

different amount of the electron beam, then subject them all to the same development process. The thickness of the remaining resist is then measured. The resulting data are used to generate a contrast curve, a plot of the remaining thickness of the resist as a function of the exposure dose, with the thickness normalized to the initial height [2, 8]. Figure 4(a) shows a contrast curve that might hypothetically be collected for a polymer resist. Note that this figure is not a plot of actual data, it is a sketch of what the collected data would look like.

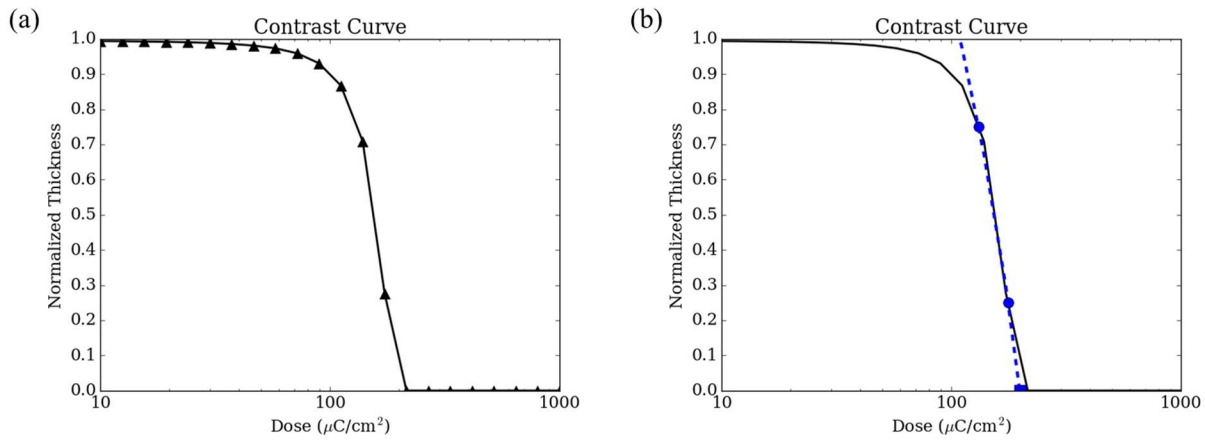

Figure 4. Contrast curves for hypothetical data. (a) Just the raw data is shown. (b) The data symbols are dropped in favor of a line fitted to the 25% and 75% thickness points. The slope of this line defines the contrast, and its dose-intercept defines the clearing dose.

Once a contrast curve is plotted, it can be analyzed to give quantitative insights into the nature of a resist. A line is drawn between the point on the curve where 75% of the resist remains in place after development and the point where 25% remains, as in Figure 4(b). The intersection of this line with the dose-axis defines the clearing dose for the resist for the initial thickness of the layer used. The term sensitivity is also used a lot in the literature to refer to the same concept, where a resist with a high clearing dose is said to have a low sensitivity, while a low clearing dose indicates a high sensitivity resist.

Another important quantity is *contrast*, defined by

$$\gamma = (\log_{10}(D_{t=0}/D_{t=1}))^{-1},$$

where $D_{t=0}$ is the dose at which a large area exposure first clears and $D_{t=1}$ is the dose below which the full thickness of the resist is retained [9]. Contrast can also be understood as the slope of the contrast curve (Figure 4) measured at the 50% thickness point [8, 9]. A resist with high contrast permits more variation in processing conditions before deviating from desired behavior (this is called process latitude). High contrast resists also tend to have a sharper cutoff between the exposed area and the unexposed area, creating a steeper sidewall in the resist layer and enabling better resolution to be achieved.

1.3.2 Interpreting the Lithographic Process

Revisiting Figure 1, we can see that the exposure to the electron beam in step 2 increases the polymer's solubility by reducing its molecular weight, in accordance with what we know about Flory-Huggins theory. Then, the development in step 3 requires a delicate balance: we need a solvent with a χ parameter that will allow it to dissolve away the broken-up chains left behind by electron beam exposure, but that will not be energetically favorable enough to dissolve away the longer chains in the unexposed polymer.

However, this interpretation is not how things are generally presented in the nanolithography literature. Instead, as I will show in the next section, the research literature mostly only compares sensitivity and contrast determined after adjusting various processing steps, without addressing the polymer physics going on at the molecular level.

1.4 Existing Research in Nanolithography

One of the generally most active areas of research in the field of nanolithography is how to make smaller features, referred to as improving the resolution of the technique. In industry terms, the cost to process a silicon wafer is roughly constant, so decreasing the size of the

features formed in the lithographic process allows more circuit elements to be printed on each wafer, yielding increased circuit complexity and higher density of circuits per wafer [10]. Additionally, certain types of features, like the field-effect transistors that make up microprocessors, work better when they are smaller, with benefits including faster operation, lower voltage requirements, and less energy dissipation [11].

However, existing approaches to investigating the effects of development conditions on the results of lithography are confusing at best.

1.4.1 Effect of Molecular Weight on Sensitivity

Yan et al. [12] investigated the effects of molecular weight on the development of PMMA. By generating contrast curves for five different molecular weights of PMMA at a variety of temperatures, they drew some conclusions about the effects of temperature and molecular weight. The contrast curves they collected are shown in Figure 5. The curves move to the right with increasing molecular weight and with decreasing temperature. The curves for different molecular weights converge at lower temperatures, and the curves at lower temperatures appear steeper. Curves of contrast and sensitivity as a function of developer temperature are also included and show higher values for lower temperatures.

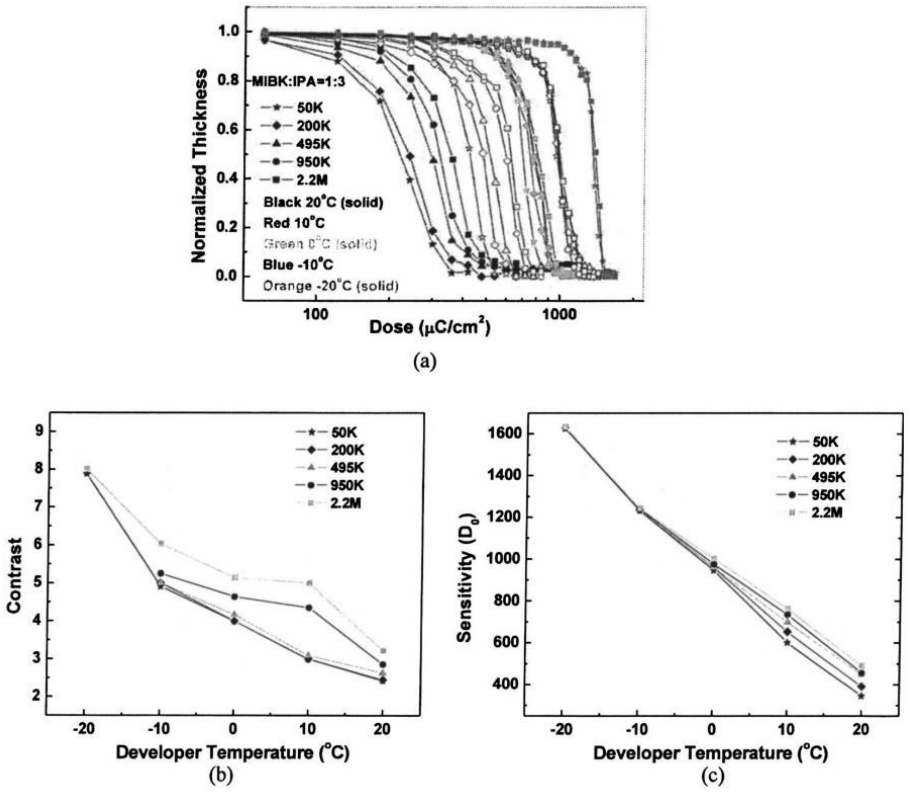

Figure 5. Various molecular weights of PMMA were developed at various temperatures in a 1:3 solution of MIBK and IPA. (a) The resulting contrast curves. (b) The corresponding contrast values (γ). (c) The corresponding sensitivities. (Reprinted with permission from [12]. Copyright 2008, American Vacuum Society.)

Yan et al. concluded that higher molecular weight PMMA had higher contrast and required a larger clearing dose. However, they also observed that the differences caused by molecular weight grew smaller and the curves converged with decreasing developer temperature, and that decreasing developer temperature caused an increase in contrast and a decrease in sensitivity (i.e., a higher clearing dose). Yan et al. attributed this behavior to the decrease in solubility, which necessitated an increase in exposure dose [12].

1.4.2 Effect of Developer Temperature

Developer temperature has been investigated as a potentially important parameter. Cord, et al. made a comprehensive study of the effects of developer temperature on the sensitivity of

PMMA [13]. Using the common 3:1 IPA:MIBK developer mixture, a standard development time of 60 seconds, and 160 nm films of PMMA, they found that decreasing the developer temperature decreased the sensitivity of positive-tone PMMA. However, once they decreased the temperature to -35°C, it became impossible to clear the PMMA from the substrate with 60 seconds of development, no matter the exposure dose.

Cord, et al. collected contrast curves for many different developer temperatures, shown in Figure 6. The decreasing solvent temperature decreased the sensitivity of the PMMA to the electron beam, as can be seen by the curves moving to the right with decreasing temperature. However, the maximum resolution that can be achieved by the lithographic process depends not on sensitivity, but rather on contrast. Cord, et al. calculated contrast γ for each curve in Figure 6, and plotted contrast as a function of temperature in Figure 7. It was observed that decreasing temperature increased contrast for positive-tone PMMA, with a maximum at about -15°C. Cord, et al. hypothesize that decreasing temperature prevents partially exposed PMMA from being rinsed away during development, thereby improving contrast. However, as temperature decreases further, it requires a larger dose of exposure to the electron beam for the PMMA to be removed during development. This causes an increasing prevalence of cross-linking in the PMMA, progressively hindering development until it becomes completely impossible at -35°C.

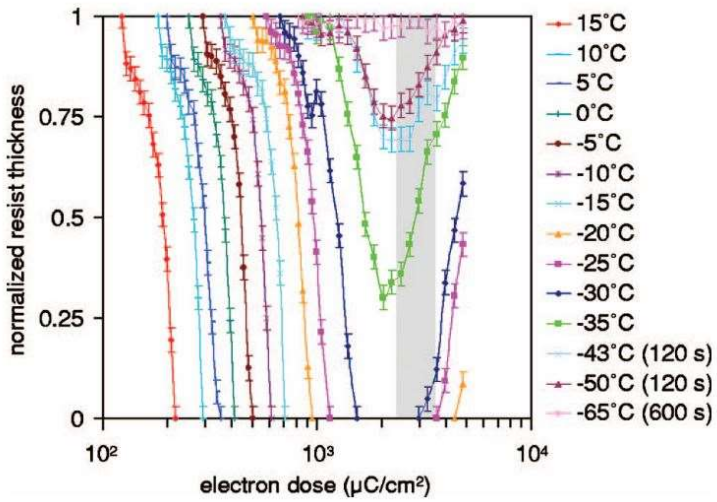

Figure 6. Contrast curves measured for PMMA developed in 3:1 IPA:MIBK at various temperatures. All samples had a predevelopment thickness of 160 nm and were developed for 60 s, unless otherwise indicated. (Reprinted with permission from [13]. Copyright 2007, American Vacuum Society.)

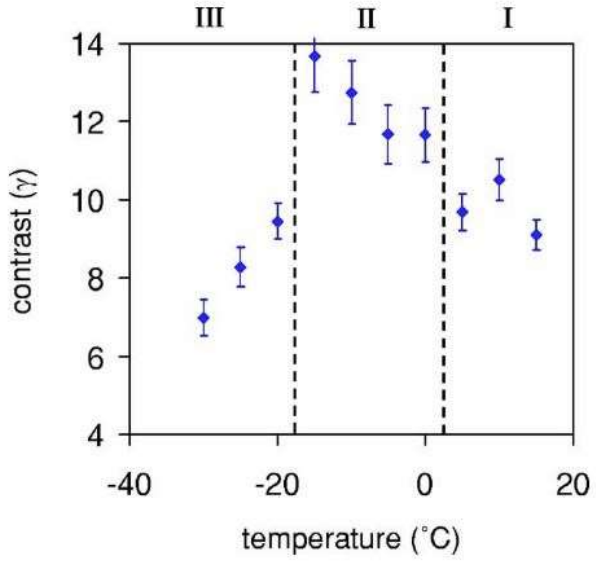

Figure 7. Contrast γ as a function of temperature, derived from the slope of the contrast curves in Figure 6. Cord, et al. describe three temperature regimes in the plot: region I, where contrast is affected by partially exposed resist at the edges of the exposure area; region II, where these partially exposed chunks are frozen in place, allowing optimal contrast; and region III, where increasing amounts of crosslinking hinder development. (Reprinted with permission from [13]. Copyright 2007, American Vacuum Society.)

1.4.3 Developer Type/Solvent Mixture

Olzierski and Raptis [14] studied the effects of different developer solvent combinations on the lithographic performance of PMMA. They compared the traditional combinations of MIBK and IPA with various mixtures of a proposed co-solvent of IPA and water (H_2O). Figure 8 presents the data they collected. They concluded that MIBK alone had very good sensitivity and moderate resolution but caused a substantial portion of the unexposed resist to dissolve as well. 1:1 MIBK:IPA was slightly less sensitive, but with much slower dissolution of unexposed resist. The standard 1:3 MIBK:IPA mixture provides negligible loss of thickness in unexposed regions, with higher contrast and moderate sensitivity. IPA alone or H_2O alone both provide low to zero sensitivity and contrast values, although when combined with relative concentration of IPA between 50% and 90%, they provide high sensitivity and contrast, comparable to the MIBK:IPA mixture. Olzierski and Raptis claim that the standard developer solution of MIBK:IPA 1:3 does not develop smoothly, and that MIBK:IPA 1:1 or IPA:H_2O 7:3 would provide higher sensitivity and more regular dissolution.

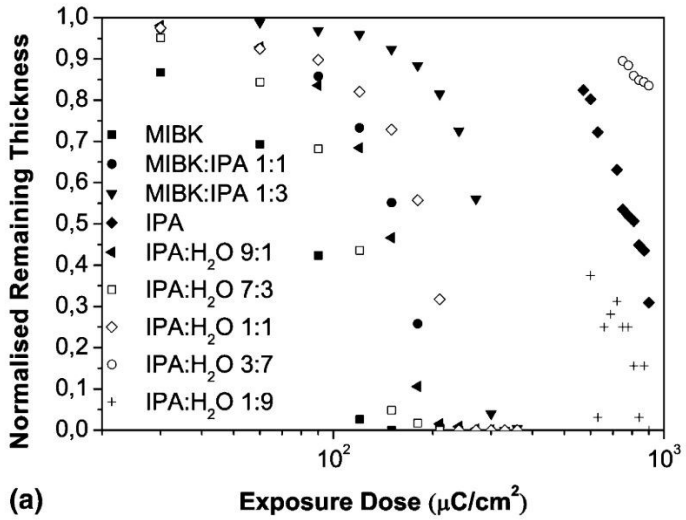

Figure 8. Contrast curves for PMMA with various relative concentrations of MIBK:IPA and IPA:H_2O developers. Initial PMMA film thickness was 460 nm and development time was 60 seconds. (Reprinted with permission from [14]. Copyright 2004, Elsevier.)

1.4.4 Dissolution Rate Studies

Kokkinis, et al. [15] conducted an experiment based on multiwavelength interferometry to study *in-situ* the dissolution process of thin polymer films. They studied molecular weights of PMMA ranging from 15 kg/mol to 996 kg/mol at thicknesses ranging from 20 nm to 300 nm in various mixtures of MIBK, IPA, and H_2O. They found similar results for 1:1 MIBK:IPA and 7:3 IPA:H_2O mixtures, with an initial period of inhibited dissolution observed for unexposed high molecular weight PMMA. Low molecular weight PMMA, as well as PMMA exposed to an electron beam in doses corresponding to the clearing dose, showed smooth dissolution. Finally, an intermediate period of inhibited dissolution was observed for films with a high initial thickness.

1.5 Goal of Thesis

Electron beam lithography is a fabrication process that is vital to the electronics industry, as well as ongoing scientific research in nanoscale systems. The solvent conditions used in the development phase of the process have an important effect on the result of the process, including the maximum resolution that can be achieved. We seek to investigate the interaction between polymer and solvent to better understand the mechanism of the development process and to improve the quality and reliability of samples produced by electron beam lithography.

To achieve this goal, we design a new sample chamber that allows samples to be measured by ellipsometry while exposed to a solvent vapor environment. We will prepare bulk films of PMMA on silicon substrates and compare how they swell in an MIBK vapor environment with how they swell in an IPA vapor environment.

Chapter 2. Experimental Methods and Development of Sample Chamber

2.1 Ellipsometry

Ellipsometry is an optical technique that allows us to determine material properties based on the changes in the polarization state of elliptically polarized light that reflects off of a sample [16]. In the ellipsometer, a quartz tungsten halogen lamp produces randomly polarized light across a broad range of visible wavelengths. This light passes through a linear polarizer and then passes through a rotating quarter-wave plate (called the compensator), causing it to become elliptically polarized [17]. The light reflects off the sample, goes through another linear polarizer (called the analyzer), and arrives at the detector. Figure 9 is an illustration of an ellipsometer.

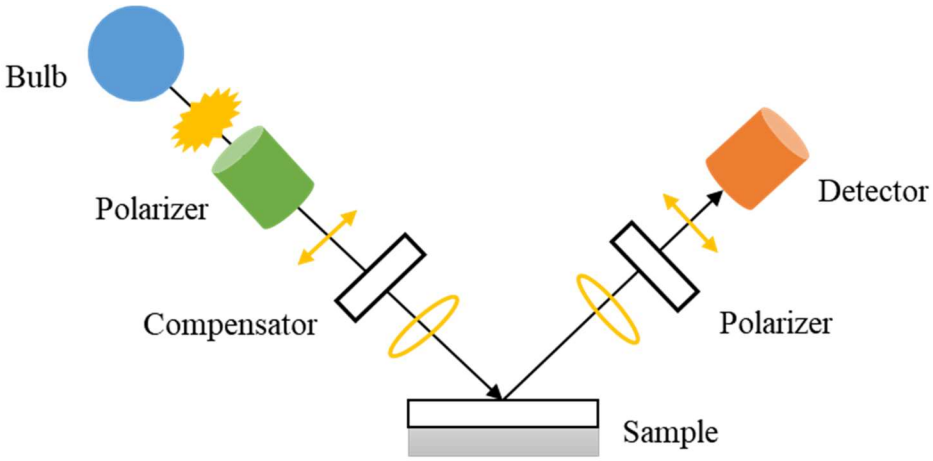

Figure 9. Illustration of an ellipsometer with a rotating compensator.

The ellipsometer measures the amplitude ratio Ψ and the phase difference Δ caused by interaction of light with the sample as a function of wavelength. These quantities are related to the complex reflectance ratio, ρ, by the fundamental equation of ellipsometry: [16]

$$\tan(\Psi)\, e^{i\Delta} = \rho \tag{2}$$

To determine the properties of our sample, we construct a model that predicts this same reflectance ratio as the ratio of the Fresnel reflection coefficients (r) for light that is polarized parallel (subscript p) or perpendicular (subscript s) to the plane of incidence:

$$\rho_{\text{model}} = \frac{r_p}{r_s}. \tag{3}$$

We model our sample as several stacked layers of material. Some layers, like the ambient air, the silicon substrate, and the native oxide layer on the substrate, have well-characterized optical properties and a known thickness. Other layers, like the polymer films we study, are not as well characterized and have unknown thickness. We model these as Cauchy layers, meaning that we assume their index of refraction, n, follows a wavelength (λ) dependence of this form: [16]

$$n(\lambda) = A + \frac{B}{\lambda^2} + \frac{C}{\lambda^4} + \cdots. \tag{4}$$

The third term and all higher-order terms are often unnecessary, so we hold C fixed or discard it entirely. Figure 10 shows the layer model we use: atop a semi-infinite silicon substrate is a thin (1.25 nm [18]) layer of silicon oxide. The polymer film sits atop this, and above the polymer is air. At each interface, some light is transmitted, and some light is reflected. The known index values for the native oxide layer and the silicon substrate are taken from the literature and provided by the ellipsometry software from the instrument's manufacturer [19–22].

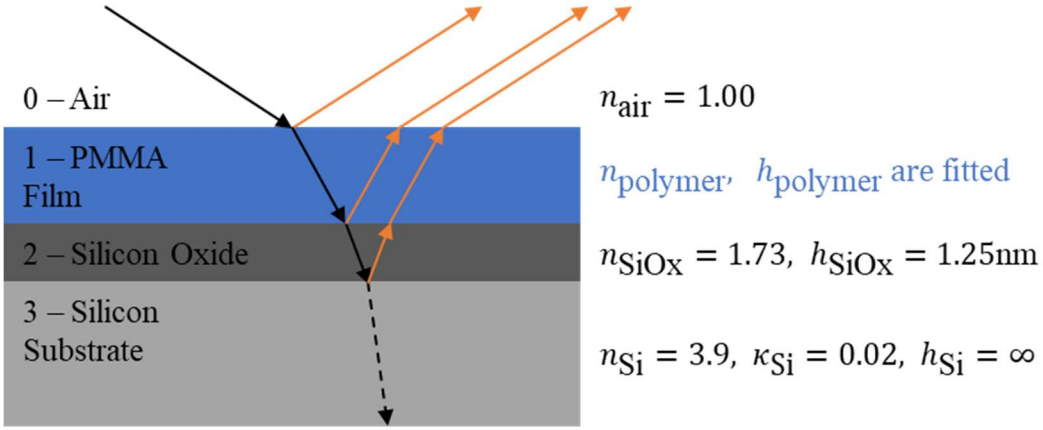

Figure 10. Diagram of the layer model for PMMA atop silicon with native oxide.

For simplicity of explanation, I will neglect the silicon oxide layer here, although it is accounted for in our model. First, consider the interface of the polymer film with the air. Snell's Law (Equation (5)) gives the relation between the angle of incidence of the incoming light and the angle at which the light is transmitted into the medium [16]. Here a subscript 0 denotes a quantity in the 0th layer, the ambient air, while subscript 1 denotes a quantity in the 1st layer of the model of the sample.

$$n_0 \sin(\phi_0) = n_1 \sin(\phi_1) \tag{5}$$

ϕ_0 is the angle of incidence of light approaching the interface from the air, measured from the normal to the surface. ϕ_1 is the angle at which the light is transmitted into the 1st layer, again measured from the normal. Due to the law of reflections (i.e., that the angle of reflection is the same as the angle of incidence), ϕ_1 is also the angle of incidence for any light that approaches the 0–1 interface from below because of a later reflection, and any light that is reflected at any point in the sample ends up leaving the sample at an angle of ϕ_0.

The Fresnel reflection coefficients for the 0–1 interface are given by the following equations, which can be derived from Maxwell's equations and the boundary conditions for a traveling electromagnetic wave: [16]

$$r_{p_{01}} = \frac{n_1 \cos(\varphi_0) - n_0 \cos(\varphi_1)}{n_1 \cos(\varphi_0) + n_0 \cos(\varphi_1)}, \qquad r_{s_{01}} = \frac{n_0 \cos(\varphi_0) - n_1 \cos(\varphi_1)}{n_0 \cos(\varphi_0) + n_1 \cos(\varphi_1)}. \tag{6}$$

We define the phase thickness β of the polymer layer, which describes how many wavelengths long it is for the light to travel through the layer [16]:

$$\beta = 2\pi \frac{h}{\lambda} n_1 \cos(\varphi_1). \tag{7}$$

The phase thickness allows us to predict how the light reflected off of the 1–2 interface (and any additional interfaces) will interfere with the light that reflected off of the higher interface. Thus, we can sum up the reflections off each interface to get the total Fresnel reflection coefficients. For our simplified two-layer system, they are as follows: [16]

$$r_{p_{\text{total}}} = \frac{r_{p_{01}} + r_{p_{12}} e^{-i2\beta}}{1 + r_{p_{01}} r_{p_{12}} e^{-i2\beta}}, \qquad r_{s_{\text{total}}} = \frac{r_{s_{01}} + r_{s_{12}} e^{-i2\beta}}{1 + r_{s_{01}} r_{s_{12}} e^{-i2\beta}}. \tag{8}$$

This is how our model predicts a value for the reflectance ratio ρ based on inputs of film thickness h and the A and B parameters that describe refractive index n. The input parameters are fitted to minimize the difference between the model's prediction for ρ and the experimentally measured value based on Ψ and Δ. This gives us very precise values for the model's input parameters. However, accuracy is subject to the reliability of the model and of the fit.

2.2 Sample Preparation

For this project, all samples were prepared using poly(methyl methacrylate) (PMMA) from Scientific Polymer Products, Inc. with molecular weight $M_w = 815\ \text{kg/mol}$ and a narrow

molecular weight distribution ($\frac{M_w}{M_n} = 1.09$). The PMMA was dissolved in toluene and spin-coated onto $2\ \text{cm} \times 2\ \text{cm}$ silicon substrates, creating layers ~300-500 nm thick. Each sample was annealed under vacuum overnight at $140°\text{C}$ to drive off all excess solvent and relax the polymer chains.

Measurements were carried out with a Woollam M2000 rotating spectroscopic ellipsometer. The wavelength range used for fitting was 400–1000 nm. The angle of incidence used was 45°. Data was collected with a five second acquisition time every 10 seconds, at double precision.

2.3 Sample Chamber Design

For this project, a special sample chamber was designed to allow each sample to be placed on the ellipsometer stage inside a solvent vapor environment. The base of the chamber allows the sample to be surrounded by a "moat" of solvent that evaporates and fills the chamber. The lid of the chamber has holes in it to allow the beam of light from the instrument to pass through at a 45° angle of incidence, while minimizing exchange of air with the rest of the room. The lid has another hole in it with a plug to allow the moat to be filled with solvent without completely removing the lid.

This design allows the sample to be placed in a solvent-rich environment without immersing the sample in solvent, which could cause the sample to wash away, and would make measurement by ellipsometry impossible. It also makes it possible to alter the solvent conditions of the environment while the sample is being measured. Figure 11 is a cross-section schematic view, illustrating the path of the ellipsometer beam.

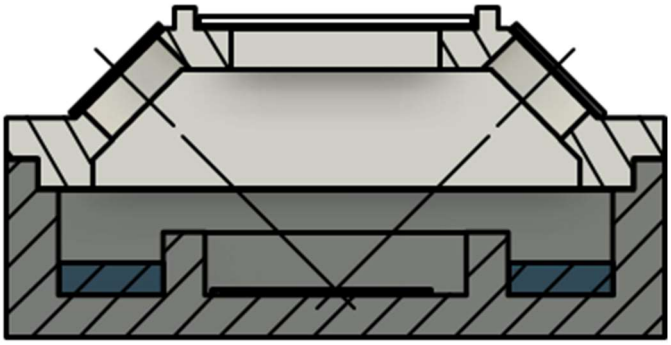

Figure 11. Schematic of the cross-section of the sample chamber through the plane of incidence of the ellipsometer beam, which has a 45° angle of incidence.

The base of the sample chamber was milled out of aluminum by the machine shop using their CNC machine. Figure 12 is an isometric view of the base of the chamber. In addition to the central area for the sample and the surrounding moat for solvent, there is a small inset at the top to help with fitting the lid.

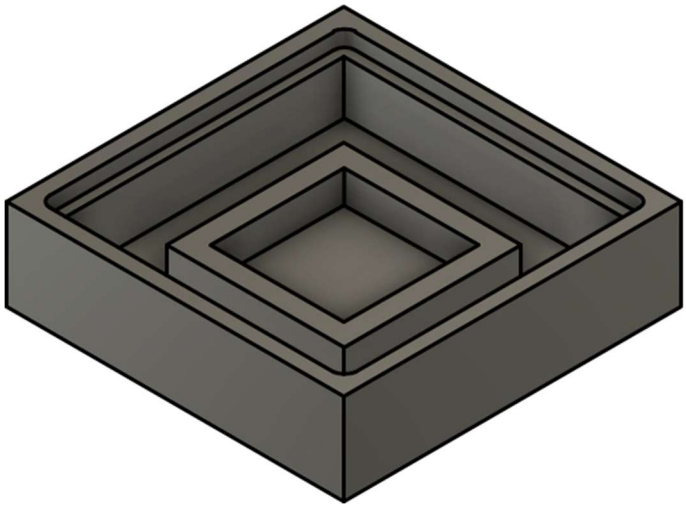

Figure 12. Isometric view of the lower portion of the sample chamber.

The upper portion of the chamber, or the lid, was specially designed to be 3D printed out of polypropylene. The lid was 3D printed using Ultimaker polypropylene filament with an average diameter of 2.85 mm. The printer used was a Lulzbot TAZ-5 with the Flexystruder Tool

Head upgrade. The build plate was heated to 100°C, and the plastic was heated to a printing temperature of 230°C. We printed on polypropylene tape with an extra wide raft (20 mm bigger than the object) to mitigate issues with the print adhering to the build plate, and we printed with a draft wall 10 mm away to reduce air currents as the print cooled. The print was made with 0.1 mm layer height, a wall thickness of 1.6 mm, and 15% infill.

Figure 13 is an isometric view of the lid. In addition to the openings for the ellipsometer beam and the solvent filler hole, the lid features a viewing window that is covered by a microscope slide, complete with rails to guide the slide in place. Circular recesses in the outside of the lid hold magnets, which allow thin strips of hole-punched metal to be held in place. These strips have a smaller hole diameter than the polypropylene lid does, further restricting exchange of air between the chamber and its surroundings. Additionally, the strips can be easily adjusted or swapped out to avoid interfering with the ellipsometry beam.

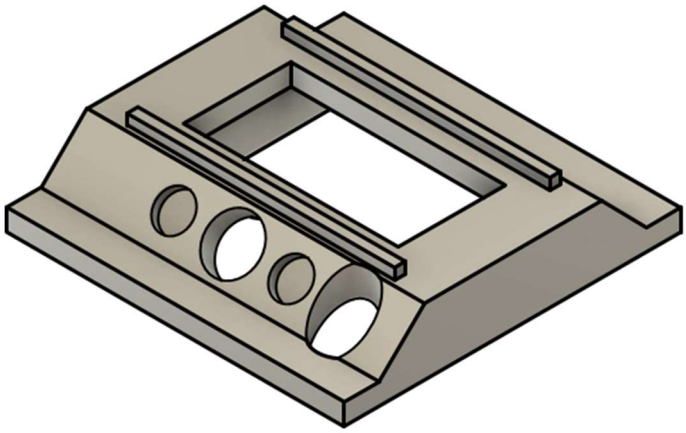

Figure 13. Isometric view of the lid of the sample chamber.

Figure 14 is a rendering of the complete design fully assembled. Fully assembled, there are several extra pieces in addition to the aluminum base and the polypropylene lid. A glass microscope slide is glued to the top with Paraloid™ B-44 to seal in the chamber while also providing a viewing window. Small magnets are fitted in the circular recesses next to the

openings for the beam path on the lid, and thin strips of metal with 7 mm diameter holes punched in them provide the final, and easily adjustable, layer of constriction around the beam path. Finally, a small plug for the solvent filler hole was also printed out of polypropylene.

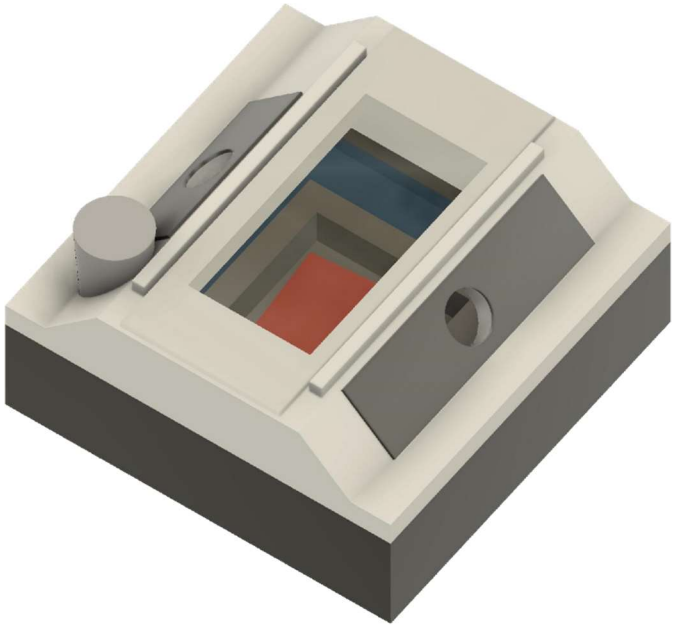

Figure 14. 3D rendering of the sample chamber, completely assembled, with a sample and solvent inside.

The full set of drawings of the sample chamber, including more schematic views, cross-section views, and all the measurements, are available in the Appendix.

Figure 15 is a photograph of the sample chamber in use. The standard ellipsometer stage was used, and the sample chamber is held in place by vacuum.

Figure 15. Photograph of the sample chamber in use on the ellipsometer.

2.4 Experimental Procedure

Each sample was placed in the sample chamber on the ellipsometer and aligned with the lid in place prior to measurement. Each sample was then measured for 5 minutes prior to the introduction of solvent into the system to establish a good baseline for the ellipsometric data. At time $t = 5$ min, 4 mL of a solvent was pipetted into the moat through the solvent filler hole in the lid. The solvent filler hole was then immediately plugged, and the sample was measured for the next 60 minutes.

Chapter 3. Results and Discussion

In this section, I will discuss various methods we used to model our samples, starting with our investigation into whether the index of refraction of the air in the chamber is an important parameter to model. I will then discuss our results for both an isopropyl alcohol (IPA) vapor environment and a methyl iso-butyl ketone (MIBK) vapor environment, and finally compare the two.

3.1 Control for Ambient Index

We conducted a control experiment with a sample of bare silicon in the sample chamber to determine the signal change caused by the solvent evaporating in the chamber, to ascertain if this change should be accounted for when modeling the effects of the solvent vapor environment on a polymer layer. After acquiring 5 minutes of baseline data, we pipetted 2 mL of IPA into the sample chamber and continued measuring the sample for another 15 minutes. While we expect a monolayer of IPA to condense onto the bare silicon substrate because the native oxide layer is a highly energetically favorable surface, the surface of a polymer film is not similarly energetically favorable, so we would not necessarily expect a monolayer to form on our polymer samples.

First, we investigate IPA. We used two versions of the layer model in Figure 16 to determine if there would be any confounding factors for modeling and fitting our polymer samples. The first model fits the thickness of an IPA monolayer condensed on the hydrophilic surface of the silicon while holding the index of refraction of IPA constant at $n_{\mathrm{IPA}} = 1.378$ [23] and holding the index of air constant at $n_{\mathrm{air}} = 1.000$. The model holds the native oxide layer thickness constant at the value measured at the start of the run by fixing the thickness of the IPA layer to $h_{0_{\mathrm{IPA}}} = 0$ nm and fitting the thickness of the native oxide layer. In this case, the

thickness of the silicon oxide layer was determined to be $h_{\mathrm{SiOx}} = 1.76$ nm. The second model is the same, except it also allows the index of refraction of the ambient medium to deviate from 1.000 as a fitting parameter to determine the change in refractive index of the air when the solvent evaporates into the chamber. The known index values for the native oxide layer and the silicon substrate are taken from the literature and provided with the ellipsometry software from the instrument's manufacturer [19–22].

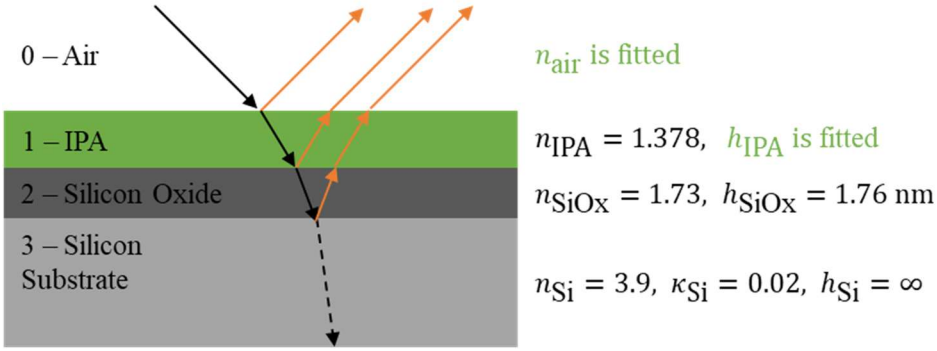

Figure 16. Layer Model of an IPA monolayer atop silicon with native oxide layer. The thickness of the silicon oxide layer was determined by measurement at the start of the run, fixing the thickness of the IPA layer to $h_{0_{\mathrm{IPA}}} = 0$ nm and fitting the thickness of the native oxide layer.

Figure 17 shows the results of our control experiment for IPA. The time axis has been shifted such that $t = 0$ is the last timestamp recorded before solvent was added to the system. Two separate tests were conducted. The first test (Figure 17(a, b)) used 2mL of IPA and a piece of silicon that was sitting around the lab with questionable cleanliness. The second test (Figure 17(c, d)) used 4 mL of IPA and a recently cut piece of silicon.

In both cases, the thickness of the IPA layer condensing on the bare silicon wafer when the solvent vapor is introduced shows a clear signal starting just after time $t = 0$. When fitting the ambient index as well as the IPA layer thickness (Figure 17(b, d)), the signal in the IPA thickness (blue) shows no appreciable change. The ambient index (green), plotted on the

secondary axis, bounces around in the region of $n_{\text{air}} = 1.0042 \pm 0.0002$ for the first sample and $n_{\text{air}} = 1.0066 \pm 1.0002$ for the second sample both before and after the introduction of IPA solvent vapor to the system. Since any effect on ambient index is clearly in the noise, we conclude that there is no need to consider the effects of ambient index in our other measurements with IPA and will hold $n_{\text{air}} = 1.000$. We speculate that the cleanliness of the silicon accounts for the overshoot in IPA layer thickness observed in Figure 17(a, b), and recommend that future work controls for the cleanliness of the silicon substrate to confirm this. In both cases, solvent was still present at the end of the test, so there should be no difference based on the volume of solvent used.

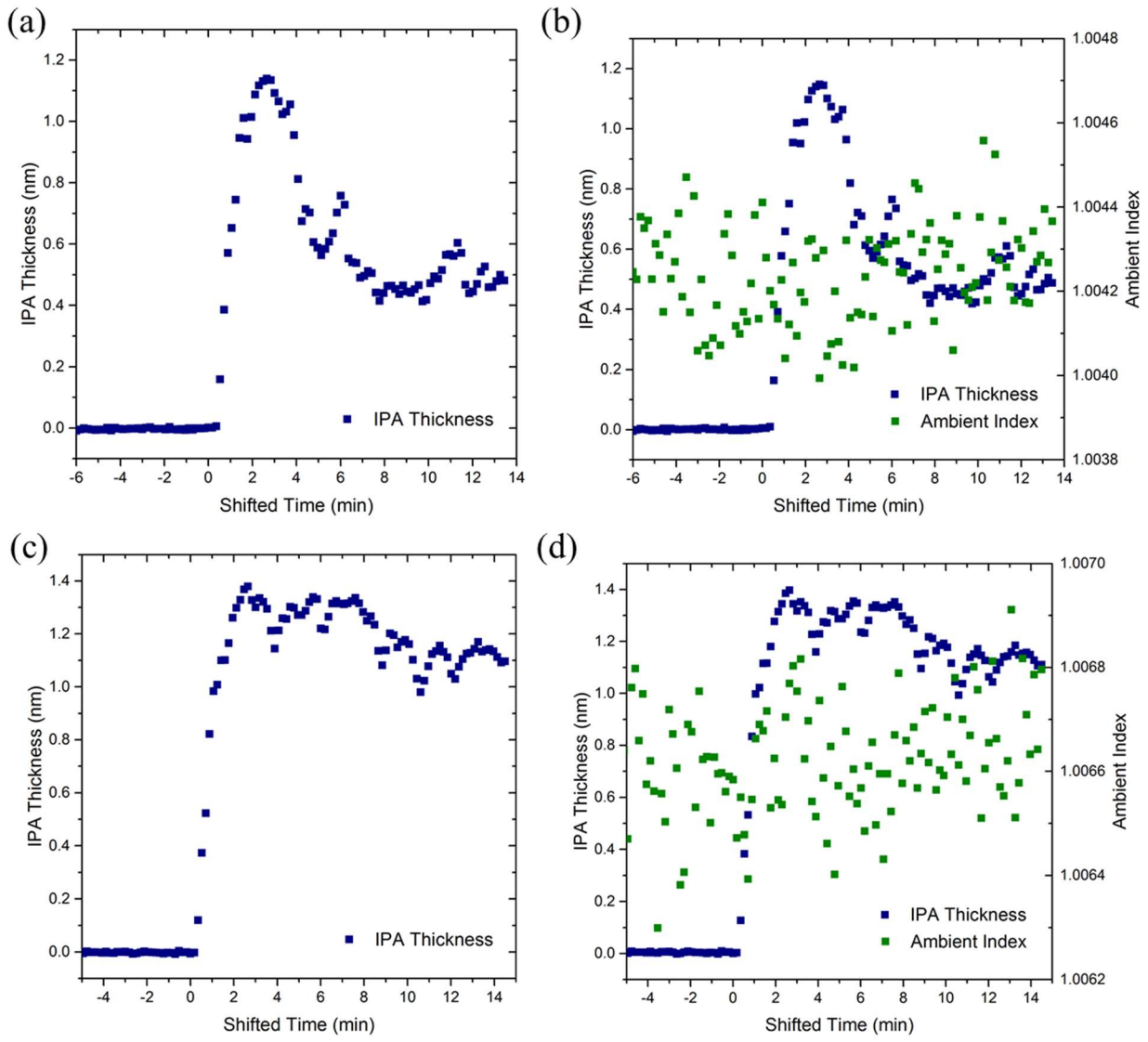

Figure 17. Parameters as a function of time for two different models of a control experiment putting a bare silicon substrate in an IPA vapor environment. Time $t = 0$ corresponds to the last timestamp before solvent was added to the system. (a) Data from the first silicon substrate tested (with questionable cleanliness) exposed to vapor from 2 mL of IPA fit to the simplest model of an IPA monolayer. (b) Data from a model that also fits the ambient index showing no change based on this additional parameter. (c) The simple monolayer model applied to data from a second, cleaner silicon sample exposed to vapor from 4 mL of IPA. (d) This second sample analyzed with the ambient index also fit in the model.

We conducted a similar control with bare silicon in the sample chamber exposed to vapor from 2mL of MIBK, using a similar model as in Figure 16, with MIBK ($n_{\mathrm{MIBK}} = 1.396$ [24]) replacing IPA. Figure 18 shows our data for this experiment. Again, the thickness of the solvent

monolayer shows a clear signal starting when the solvent is added to the chamber for both models, while any change in ambient index falls within the noise. From this, we conclude that fitting ambient index is not meaningful for the case of MIBK, as in the case of IPA.

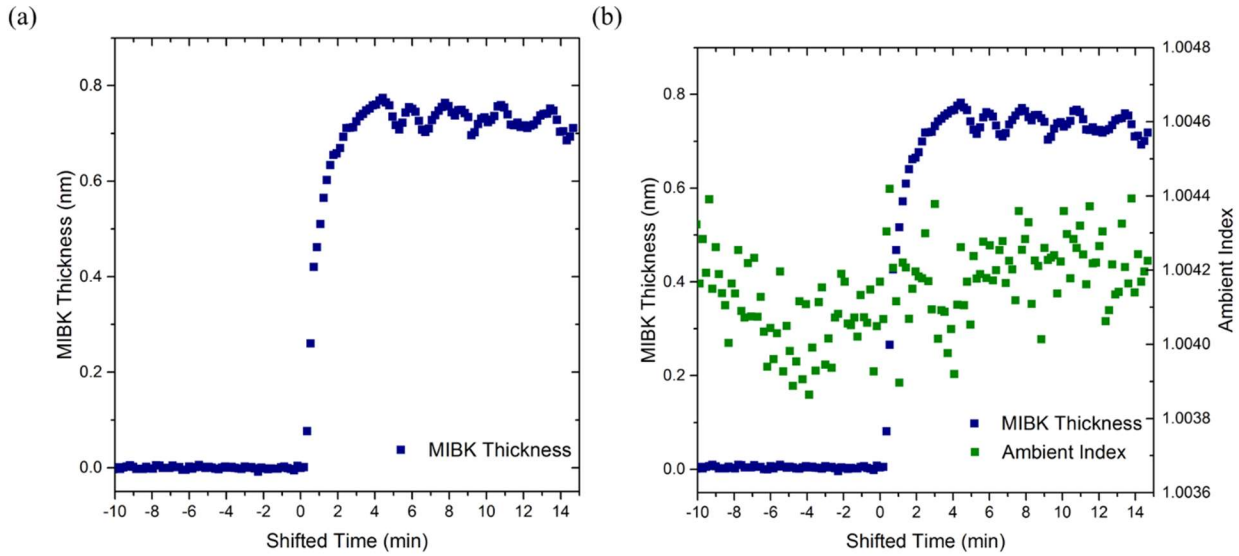

Figure 18. Data for a control experiment with bare silicon in an MIBK vapor environment. Time $t = 0$ corresponds to the last timestamp before solvent was added to the system. (a) The data fit to the simplest model of an MIBK monolayer. (b) The data from a model that also fits the ambient index shows no change based on this additional parameter.

3.2 PMMA + IPA

We have collected data for five different samples of PMMA films on silicon exposed to an IPA vapor environment. After collecting five minutes of baseline data, 4 mL of IPA was pipetted into the sample chamber and the samples were measured for the following hour. Figure 19 is a compilation plot of our data. The time axis was shifted such that the last time stamp where data was collected before addition of solvent to the chamber became time $t = 0$. Sample thickness was normalized to the mean thickness recorded over the 5 minutes of measurement before the solvent was introduced. All samples were spin-cast from toluene and have an initial thickness of 300-400 nm.

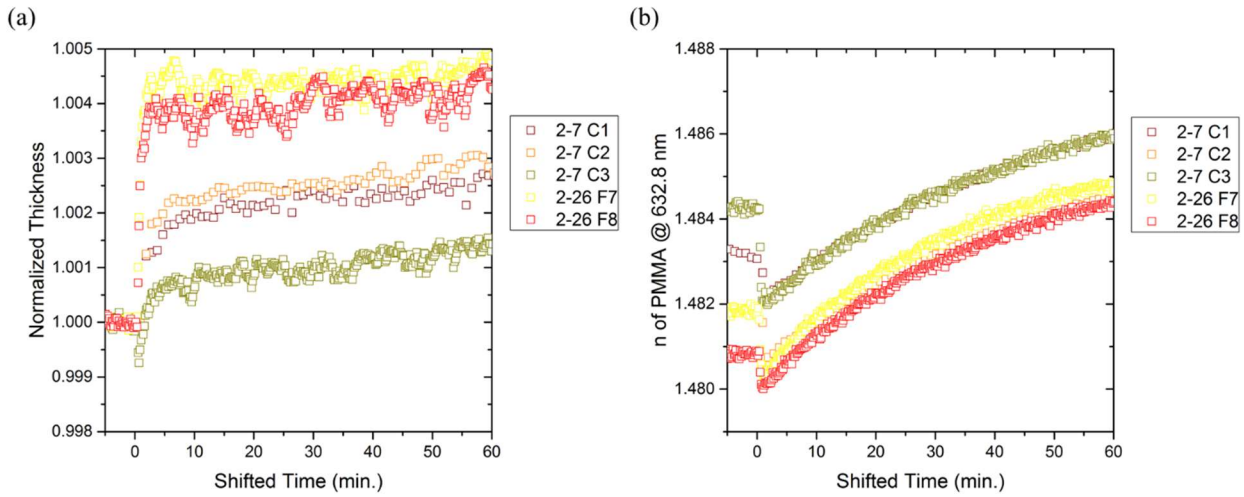

Figure 19. Data from five different samples of PMMA exposed to an IPA vapor environment. All samples were spin-cast from toluene, and have an initial thickness from 300-400 nm. (a) Sample thickness normalized to the average thickness for 5 minutes before solvent exposure as a function of time. (b) Index of refraction as a function of time.

These samples were analyzed using the layer model illustrated in Figure 10, with the index of the polymer layer obeying the Cauchy wavelength dependence given by equation (4). Although this is the simplest possible model of the system and unlikely to be the best way to model the data, it is a good starting point.

The trends in thickness and index after the solvent vapor environment has been created seem to be reproducible. However, the initial changes to layer thickness and refractive index do not appear to be consistent among this group of samples. It is surprising that index of refraction increases over time, as IPA has a smaller index ($n_{\mathrm{IPA}} \approx 1.38$) than PMMA does ($n_{\mathrm{PMMA}} \approx 1.48$).

To better understand the data, we re-normalized the thickness and index to their average values in the first 5 minutes after the solvent was introduced. Figure 20 shows the re-normalized data. By normalizing the data after the solvent has been added, the curves of thickness and index versus time for the different samples converge. We can see a steady linear growth of layer thickness, while index of refraction also increases over time.

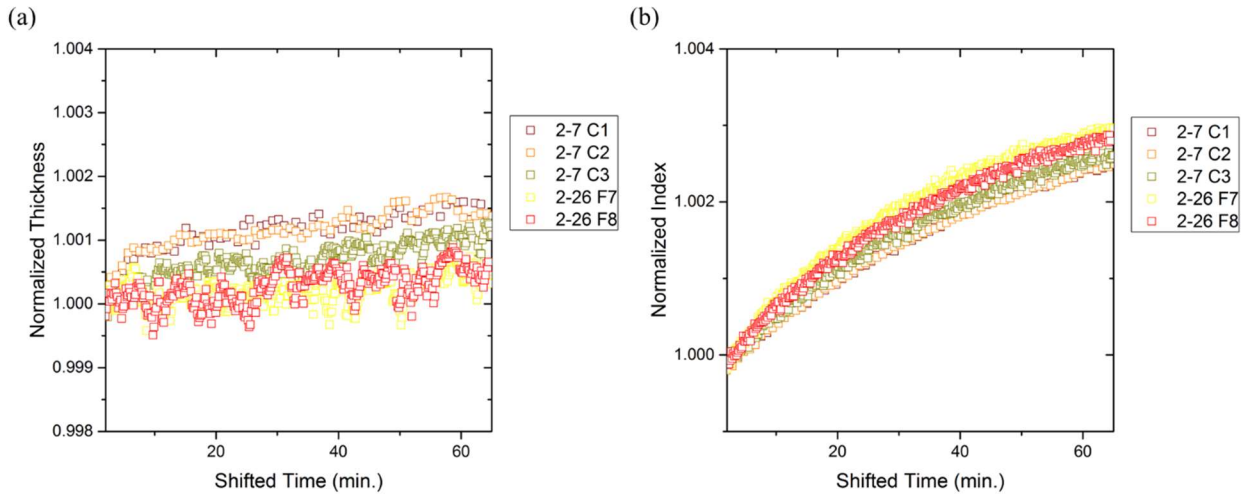

Figure 20. Data from five different samples of PMMA exposed to an IPA vapor environment. All samples were spin-cast from toluene, with initial thickness from 300-400 nm. (a) Sample thickness normalized to the average thickness for the 5 minutes after solvent exposure as a function of time. (b) Index of refraction normalized to the average for the 5 minutes after solvent exposure as a function of time.

3.2.1 Alternate Fitting Method

We introduce a new variation of the layer model to better describe the dynamics of this system. In this model, the layer of PMMA is replaced with an effective medium approximation (EMA). The EMA model holds the optical constants of both PMMA and IPA fixed, and fits the total thickness of a layer composed of both substances as well as what the proportion of IPA to PMMA is in the layer [25, 26]. The optical constants of PMMA are determined by fitting the Cauchy equation coefficients for PMMA for the five minutes before exposure to the solvent while holding the proportion of IPA in the EMA at 0. Each sample's values were slightly different, but across all the samples created in this study, we found the Cauchy equation coefficients of PMMA to be $A_{\mathrm{PMMA}} = 1.4709 \pm 0.0008$ and $B_{\mathrm{PMMA}} = 0.00452 \pm 0.00009$. The PMMA's optical properties are then fixed to the sample's fitted values, and the data is refit for the whole run allowing the concentration of IPA to vary.

As previously, the thickness of the native oxide layer is held at the accepted value in the literature (1.25 nm [18]) . The known index values for the native oxide layer and the silicon substrate are taken from the literature and provided with the ellipsometry software from the instrument's manufacturer [19–22].

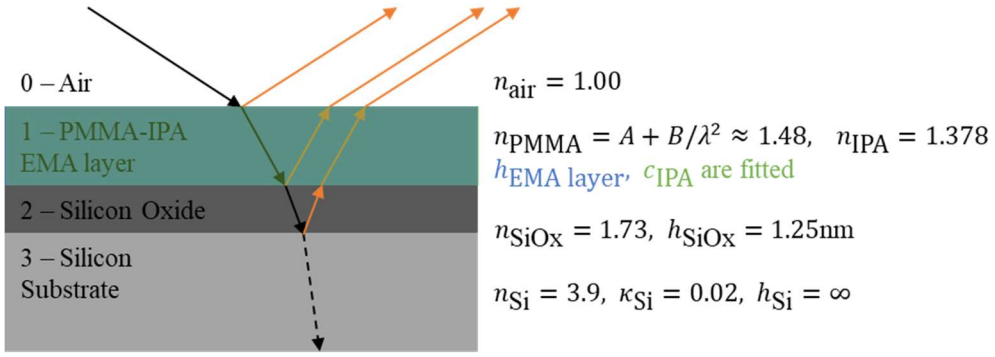

Figure 21. EMA Layer Model of IPA penetrating PMMA atop silicon with native oxide layer. The optical properties of the PMMA were determined by measurement at the start of the run, fixing the concentration of IPA in the EMA to $c_{0_{IPA}} = 0\%$ and fitting A and B of the PMMA.

Figure 22 shows the results of the EMA model. Figure 22(a) plots thickness of the EMA layer normalized before addition of solvent as a function of time. The percent thickness changes by a variable amount for each sample right after the addition of solvent, and then begins a steady upward trend. Figure 22(b) plots the percentage of the EMA made of IPA as a function of time. Since each sample of PMMA's optical properties were determined independently before the addition of solvent, all the samples show agreement that there is no IPA in the EMA before IPA was added to the sample chamber. Upon the addition of IPA to the sample chamber, the proportion of IPA in the EMA spikes up for all samples, before declining to a negative value. Evidently, the EMA model is not a viable way to interpret the results of exposing our samples to IPA vapor.

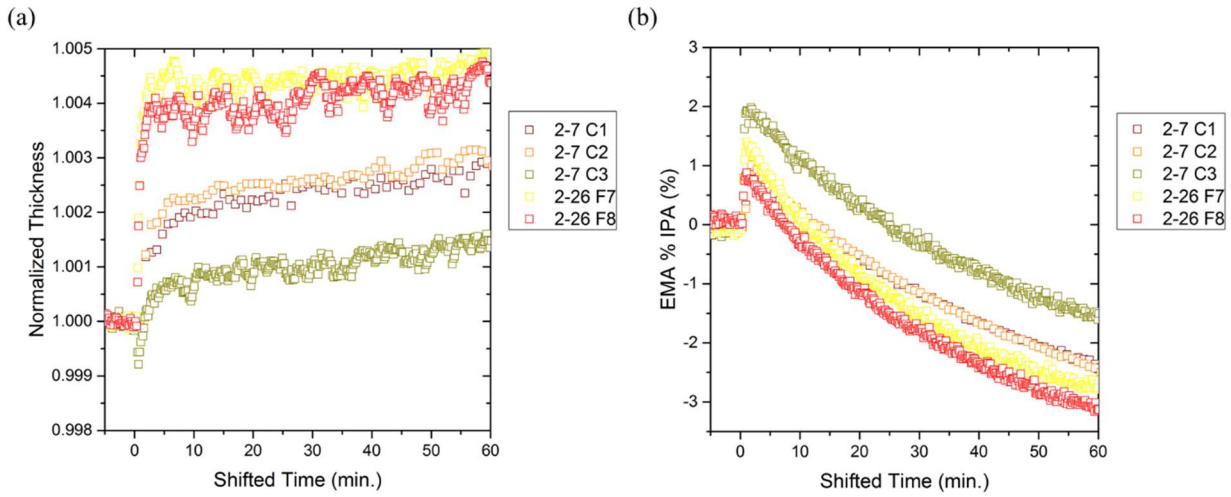

Figure 22. Data from five different samples of PMMA exposed to an IPA vapor environment. Samples were modeled with an EMA composed of PMMA and IPA. All samples were spin-cast from toluene, with initial thickness from 300-400 nm. (a) Sample thickness normalized to the average thickness for the 5 minutes before solvent exposure as a function of time. (b) IPA concentration as a function of time.

Despite this, the fit of the data is good. Figure 23 shows a representative set of curves of the measured and modeled spectroscopic ellipsometric data (The data correspond to time $t = 57$ minutes for the sample labeled "2-26 F8"). Ψ is plotted in red on the left axis, and Δ is plotted in green on the right axis. The modeled data (solid black line) shows excellent agreement with the experimental data, although the EMA composition predicted by the model at this time is -3.0%.

Future work can look at finding a more meaningful model to interpret this data. Based on work by Ogieglo, et al. [26], it may be worth trying a layer model with the PMMA separated into a top swollen (EMA) layer and a bottom layer of pure PMMA free of solvent. This would correspond to Case II diffusion of the solvent into the polymer film [27].

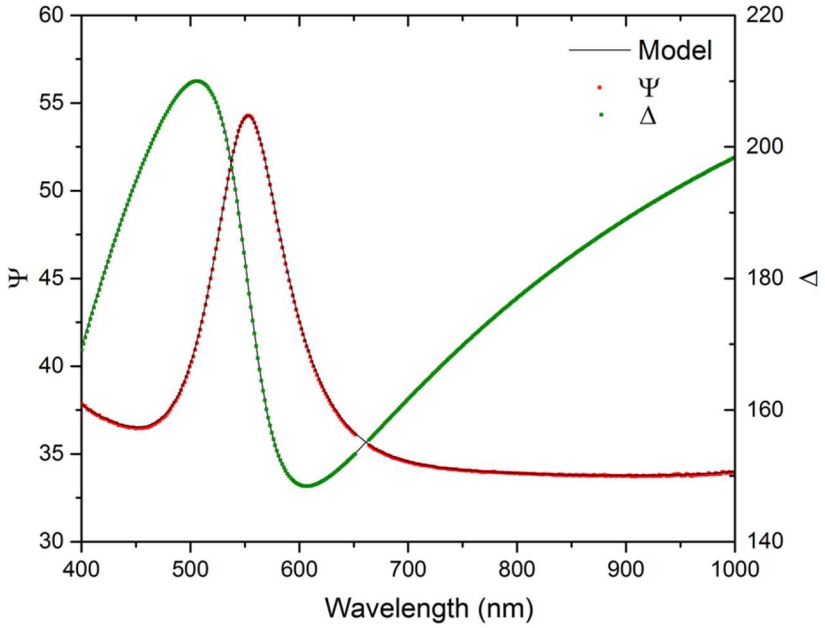

Figure 23. Representative curves of Psi and Delta for a sample in an IPA vapor environment, corresponding to time $t = 57$ minutes for the sample labeled "2-26 F8" in Figure 22. Despite the excellent fit of the model to the data, these curves predict -3% IPA in the EMA layer.

3.3 PMMA + MIBK

We have collected data for four different samples of PMMA films on silicon that were exposed to an MIBK vapor environment. All four samples were cast from toluene to a thickness of ~310-320 nm. We model these samples in similar fashion to the samples exposed to IPA: with an EMA model composed of PMMA that follows the Cauchy equation and MIBK with its index held fixed at $n_{\mathrm{MIBK}} = 1.396$. The optical properties of PMMA were determined for each sample by fitting the five minutes prior to the addition of MIBK to the sample chamber with the assumption that no MIBK was present in the EMA.

Figure 24 shows the results of exposing PMMA to MIBK vapor. Figure 24(a) plots thickness (normalized before addition of solvent) as a function of time. Once again, the time axis has been defined such that time $t = 0$ is the last timestamp recorded before starting to add solvent to the sample chamber. All samples show a sharp increase in thickness immediately

following the addition of MIBK to the system, followed a slower linear trend upward. Figure 24(b) shows the percentage of the EMA layer that is MIBK. Once again, the technique for fitting the optical properties of PMMA assures that the EMA is 0% MIBK until MIBK is added to the sample chamber. All samples show a rapid increase in MIBK concentration, followed by a slow decrease and leveling off. The EMA ends up being composed of 1.0-3.0% MIBK after an hour in the vapor environment in the sample chamber. The initial spike in MIBK concentration observed in Figure 24(b), followed by the slow decay, suggests that perhaps MIBK is first condensing on the surface of the PMMA film before dissolving into the film. Future work can adjust the layer model to test for this.

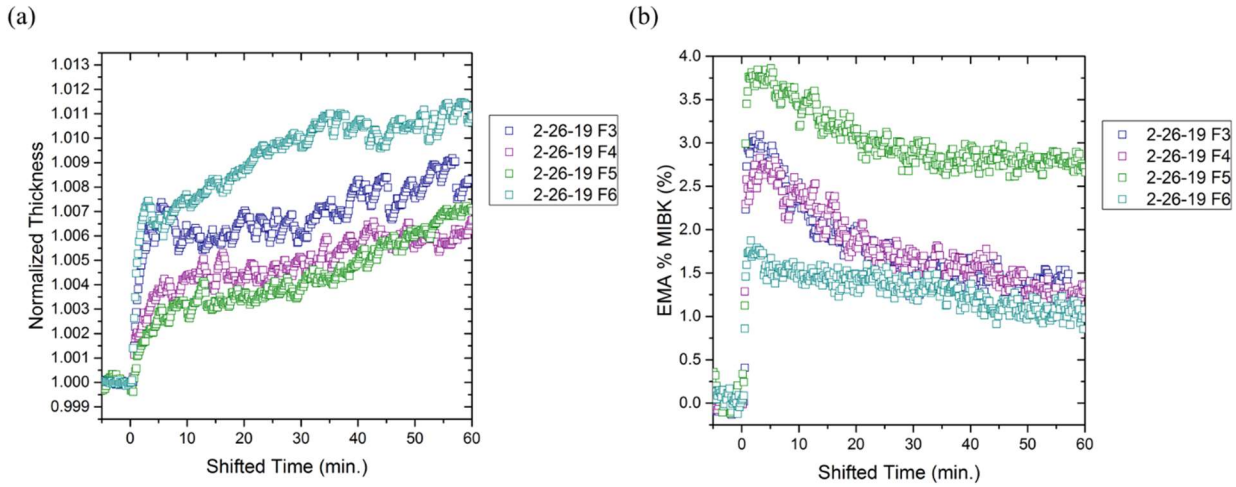

Figure 24. Data from four different samples of PMMA exposed to an MIBK vapor environment. Samples were modeled with an EMA composed of PMMA and MIBK. All samples were spin-cast from toluene, with initial thickness from 310-320 nm. (a) Sample thickness normalized to the average thickness for the 5 minutes before solvent exposure as a function of time. (b) MIBK concentration as a function of time.

3.4 Comparison of MIBK and IPA

We now compare the results for the two different solvents. For this comparison, we used the EMA model for both solvent conditions. Although the predicted concentration of IPA is nonsensical, the determined values for film thickness and index of refraction (calculated based

on the proportion of IPA to MIBK in the EMA) are unaffected. Figure 25(a) plots the measured film thickness as a function of time, normalized after the addition of solvent. The square symbols indicate samples exposed to an MIBK vapor environment, while the triangles indicate samples exposed to an IPA vapor environment. The samples exposed to MIBK show a faster increase in film thickness than the samples exposed to IPA. This makes sense, since MIBK is a good solvent for PMMA, while IPA is a non-solvent [14, 28]. Figure 25(b) plots the index of refraction as a function of time, normalized after the addition of solvent. Again, we can see clearly distinct trends in the behaviour of the samples under different solvent conditions. Samples in an IPA vapor environment show a much greater increase in index of refraction than samples in an MIBK vapor environment.

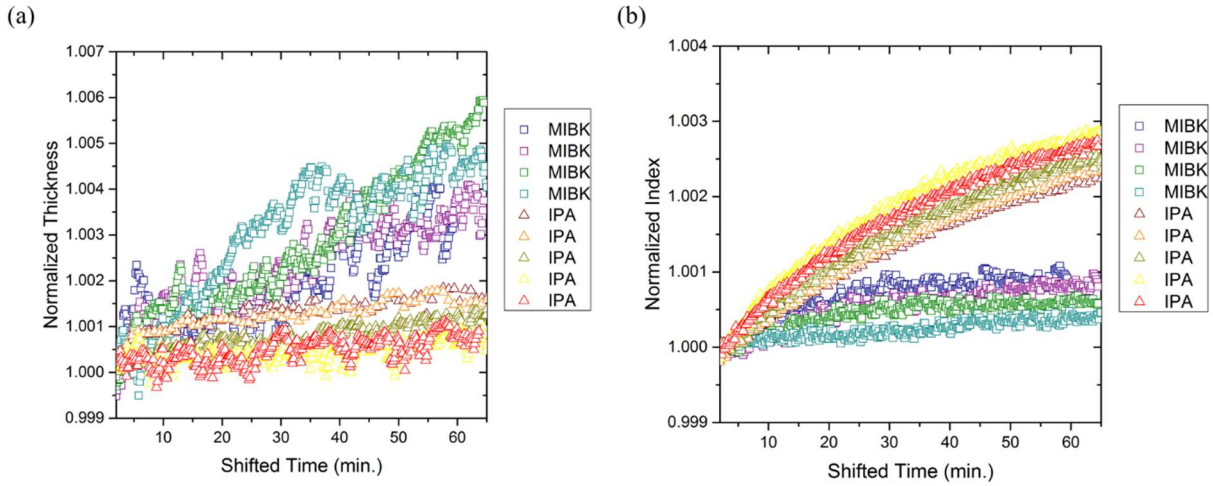

Figure 25. Comparison of data from PMMA films exposed to MIBK or IPA vapor environments. Samples were modeled with an EMA composed of PMMA and solvent. All samples were spin-cast from toluene, with initial thickness from 300-400 nm. (a) Sample thickness normalized to the average thickness for the 5 minutes before solvent exposure as a function of time. (b) Calculated index of refraction for the EMA layer as a function of time.

Chapter 4. Summary and Conclusions

This work set out to investigate the interaction between polymer and solvent as used in the nanolithographic process. We designed and fabricated a new sample chamber that allows the swelling of polymer films upon exposure to solvent vapor-saturated environments to be measured by spectroscopic ellipsometry.

We used silicon wafers with a native oxide layer as a control to measure the effects of solvent vapor saturation on the index of refraction of air and found the effects to be negligible.

We measured the swelling of PMMA films exposed to IPA vapor and MIBK vapor environments. We found that an EMA model was successful in modeling PMMA exposed to MIBK vapor, but provided unphysical results for PMMA exposed to IPA vapor. We also observed that PMMA swelled faster in the MIBK environment than the IPA environment, which aligns with our expectations.

Future work will work towards improving the ellipsometer layer model fitting, and can explore solvent mixtures as well as other solvents, like the 7:3 IPA:H_2O co-solvent mixture suggested by the nanolithography literature [14].

References

[1] S. Landis, *Nano-lithography*. London: ISTE, 2011.

[2] S. Cabrini and S. Kawata, *Nanofabrication handbook*. CRC Press, 2012.

[3] C. B. Walsh and E. I. Franses, "Ultrathin PMMA films spin-coated from toluene solutions," *Thin Solid Films*, vol. 429, no. 1–2, pp. 71–76, Apr. 2003.

[4] A.-P. Blanchard-Dionne and M. Meunier, "Electron beam lithography using a PMMA/P(MMA 8.5 MAA) bilayer for negative tone lift-off process," *J. Vac. Sci. Technol. B, Nanotechnol. Microelectron. Mater. Process. Meas. Phenom.*, vol. 33, no. 6, p. 061602, Nov. 2015.

[5] P. C. Hiemenz and T. P. Lodge, *Polymer Chemistry, Second Edition*. CRC Press, 2007.

[6] C. Roth and R. Baglay, "Fundamentals of polymers and glasses," in *Polymer Glasses*, Boca Raton, FL: CRC Press, 2016, pp. 1–22.

[7] C. Roth, J. Pye, and R. Baglay, "Correlating glass transition and physical aging in thin polymer films," in *Polymer Glasses*, Boca Raton, FL: CRC Press, 2016, pp. 181–204.

[8] A. A. Tseng, *Nanofabrication : fundamentals and applications*. World Scientific, 2008.

[9] G. P. Wiederrecht, *Handbook of nanofabrication*. Elsevier, 2010.

[10] B. Holt, "Facing the Hot Chip challenge (again)," in *2005 IEEE Hot Chips XVII Symposium (HCS)*, 2005, pp. 1–44.

[11] K. R. Sharma, *Nanostructuring operations in nanoscale science and engineering*. McGraw-Hill, 2010.

[12] M. Yan, S. Choi, K. R. V. Subramanian, and I. Adesida, "The effects of molecular weight on the exposure characteristics of poly(methylmethacrylate) developed at low temperatures," *J. Vac. Sci. Technol. B Microelectron. Nanom. Struct.*, vol. 26, no. 6, pp. 2306–2310, 2008.

[13] B. Cord, J. Lutkenhaus, and K. K. Berggren, “Optimal temperature for development of poly(methylmethacrylate),” *J. Vac. Sci. Technol. B Microelectron. Nanom. Struct.*, vol. 25, no. 6, pp. 2013–2016, Dec. 2007.

[14] A. Olzierski and I. Raptis, “Development and molecular-weight issues on the lithographic performance of poly (methyl methacrylate),” *Microelectron. Eng.*, vol. 73–74, pp. 244–251, Jun. 2004.

[15] A. Kokkinis, E. S. Valamontes, D. Goustouridis, T. Ganetsos, K. Beltsios, and I. Raptis, “Molecular weight and processing effects on the dissolution properties of thin poly(methyl methacrylate) films,” *Microelectron. Eng.*, vol. 85, no. 1, pp. 93–99, 2008.

[16] H. G. Tompkins, *A User’s Guide to Ellipsometry*. Dover Publications, 2006.

[17] J. A. Woollam, *Guide to using WVASE32*. 2002.

[18] X. Huang and C. B. Roth, “Changes in the temperature-dependent specific volume of supported polystyrene films with film thickness,” *J. Chem. Phys.*, vol. 144, no. 23, p. 234903, Jun. 2016.

[19] C. Schinke *et al.*, “Uncertainty analysis for the coefficient of band-to-band absorption of crystalline silicon,” *AIP Adv.*, vol. 5, no. 6, p. 067168, Jun. 2015.

[20] M. A. Green, “Self-consistent optical parameters of intrinsic silicon at 300 K including temperature coefficients,” *Sol. Energy Mater. Sol. Cells*, vol. 92, no. 11, pp. 1305–1310, Nov. 2008.

[21] D. E. Aspnes and A. A. Studna, “Dielectric functions and optical parameters of Si, Ge, GaP, GaAs, GaSb, InP, InAs, and InSb from 1.5 to 6.0 eV,” *Phys. Rev. B*, vol. 27, no. 2, pp. 985–1009, Jan. 1983.

[22] W. Paulson, B. Johs, C. M. Herzinger, W. A. McGahan, and J. A. Woollam,

"Ellipsometric determination of optical constants for silicon and thermally grown silicon dioxide via a multi-sample, multi-wavelength, multi-angle investigation," *J. Appl. Phys.*, vol. 83, no. 6, pp. 3323–3336, 2002.

[23] J. Volk, T. Le Grand, I. Bársony, J. Gombköto, and J. J. Ramsden, "Porous silicon multilayer stack for sensitive refractive index determination of pure solvents," *J. Phys. D. Appl. Phys.*, vol. 38, no. 8, pp. 1313–1317, Apr. 2005.

[24] D. M. Cowan, G. H. Jeffery, and A. I. Vogel, "Physical properties and chemical constitution. Part V. Alkyl ketones," *J. Chem. Soc.*, no. 0, pp. 171–176, Jan. 1940.

[25] H. Fujiwara, *Spectroscopic Ellipsometry: Principles and Applications*. John Wiley & Sons, 2007.

[26] W. Ogieglo, H. Wormeester, M. Wessling, and N. E. Benes, "Temperature-induced transition of the diffusion mechanism of n-hexane in ultra-thin polystyrene films, resolved by in-situ Spectroscopic Ellipsometry," *Polymer*, vol. 54, no. 1, pp. 341–348, 2013.

[27] J. S. Papanu, D. S. S. Soong, A. T. Bell, and D. W. T. Hess, "Transport Models for Swelling and Dissolution of Thin Polymer Films," *J. Appl. Polym. Sci.*, vol. 38, pp. 859–885, 1989.

[28] D. G. Hasko, S. Yasin, and A. Mumtaz, "Influence of developer and development conditions on the behavior of high molecular weight electron beam resists," *J. Vac. Sci. Technol. B Microelectron. Nanom. Struct.*, vol. 18, no. 6, pp. 3441–3444, 2000.

Appendix

This appendix contains all the design drawings for the sample chamber. These drawings were generated via Autodesk Fusion360, and are all 1:1 scale with the actual sample chamber if printed on 8.5” x 11” paper.

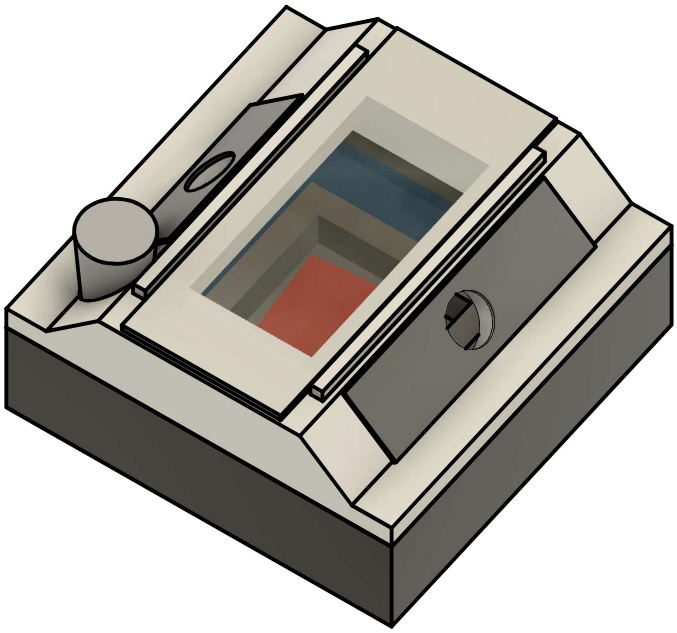

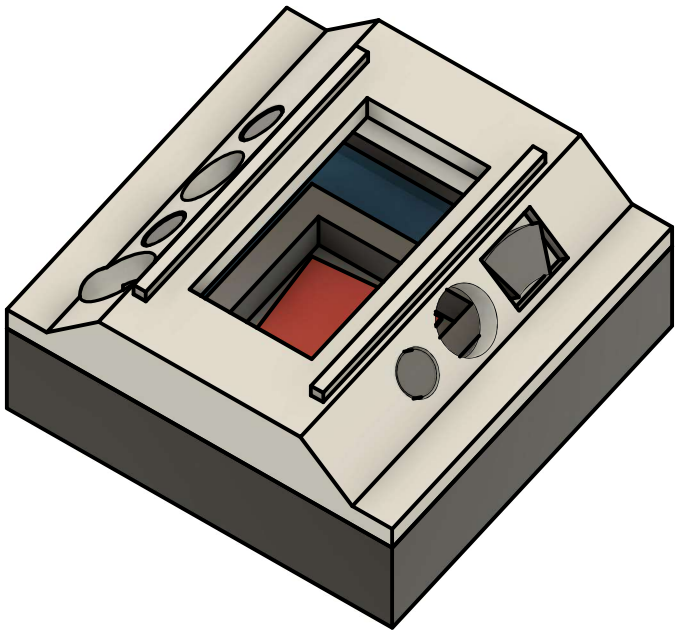

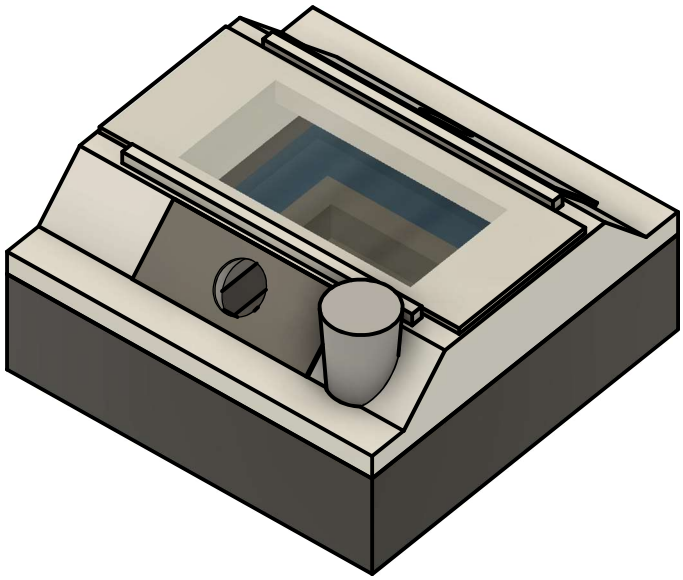

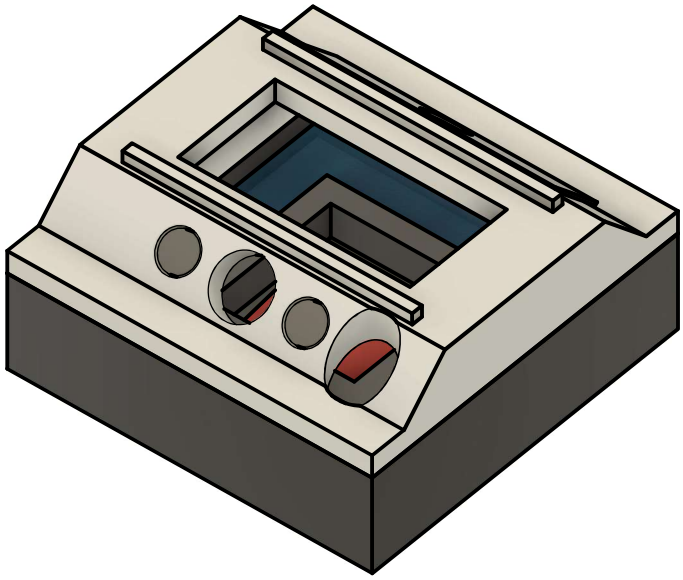

PROJECT

Sample Chamber

TITLE

Assembly

APPROVED	SIZE	CODE	DWG NO	REV
CHECKED	A			
DRAWN Alan Rohrbach 1/17/2019	SCALE 1:1	WEIGHT	SHEET 1/4	

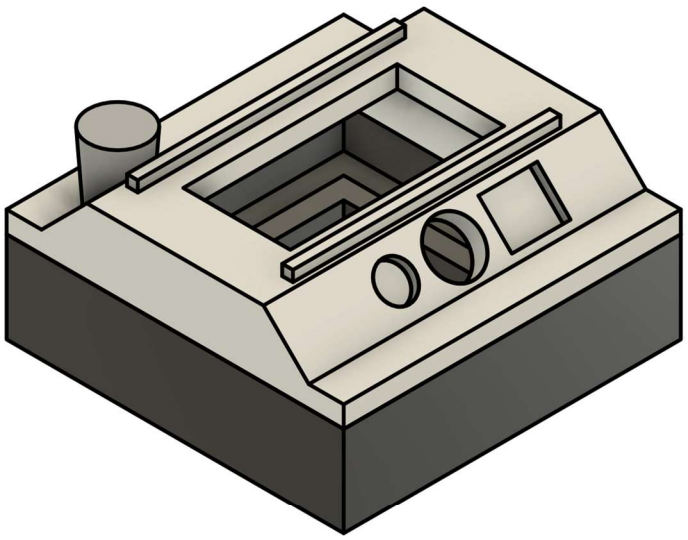

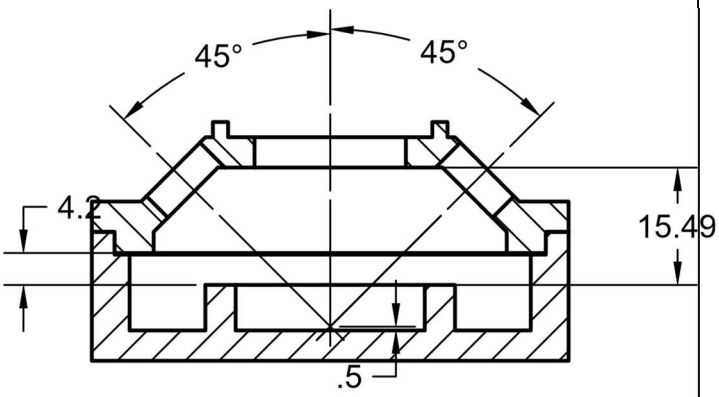

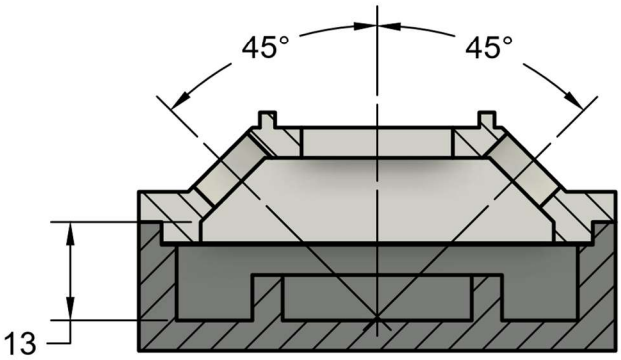

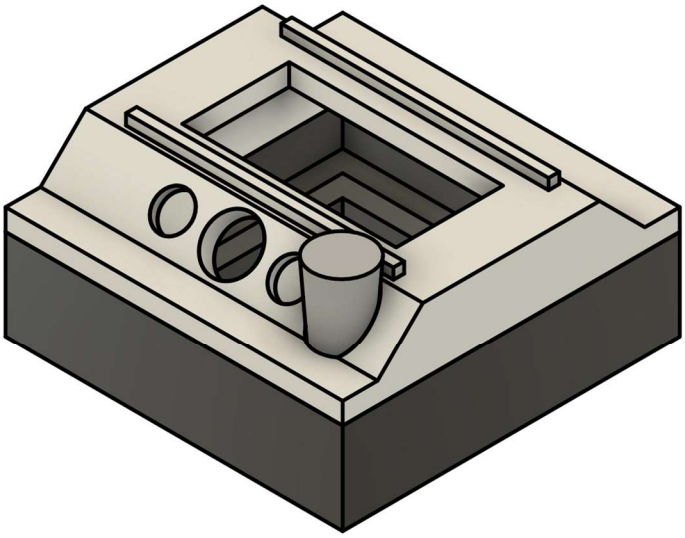

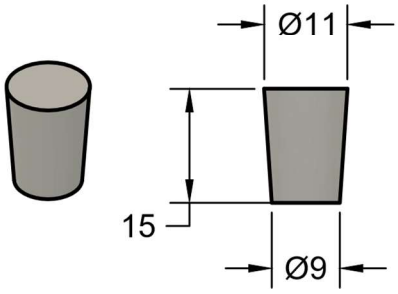

All units in millimeters

PROJECT

Sample Chamber

TITLE

Assembly

APPROVED	SIZE	CODE	DWG NO	REV
CHECKED	A			
DRAWN Alan Rohrbach 1/17/2019	SCALE 1:1	WEIGHT	SHEET 2/4	

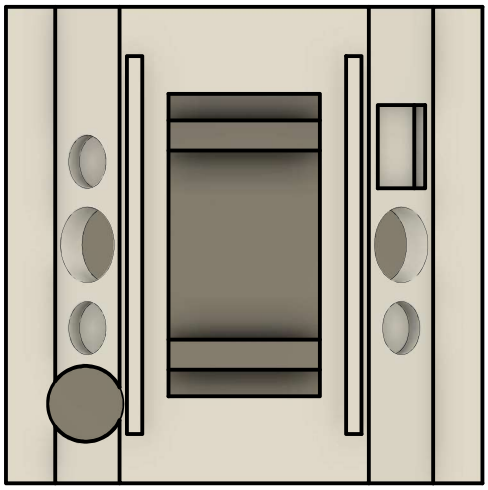

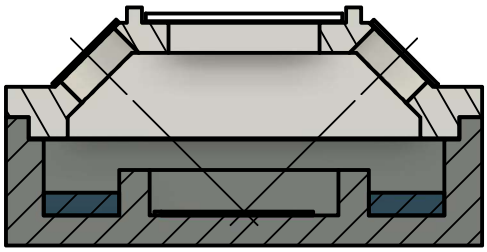

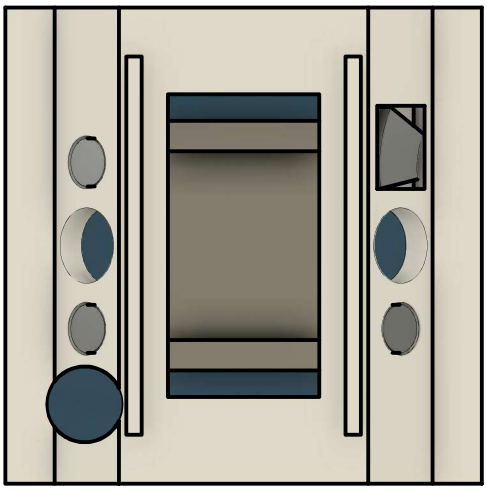

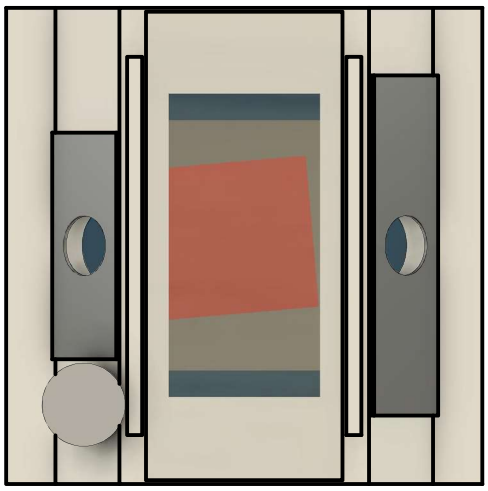

PROJECT

Sample Chamber

TITLE

Assembly

APPROVED	SIZE	CODE	DWG NO	REV
CHECKED	A			
DRAWN Alan Rohrbach 1/17/2019	SCALE 1:1	WEIGHT	SHEET 3/4	

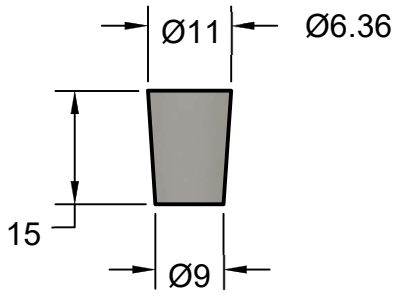

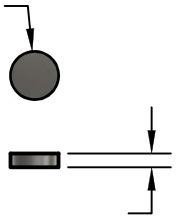

R9

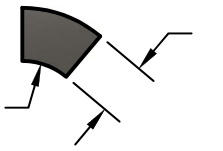

7

1.83

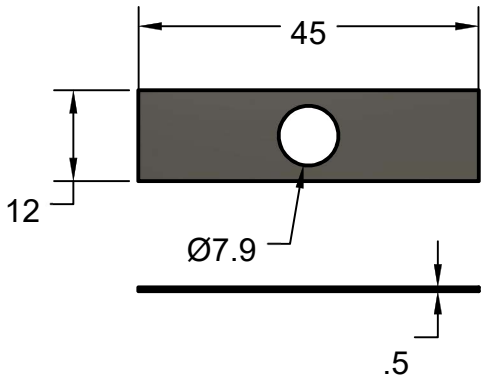

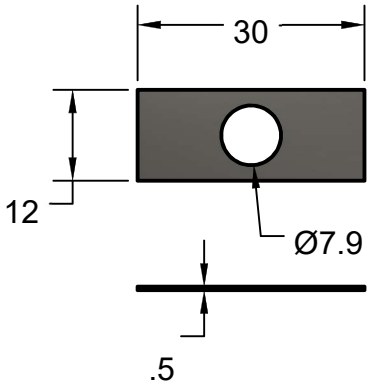

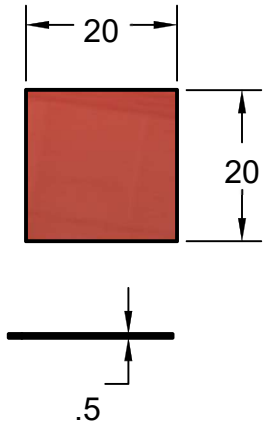

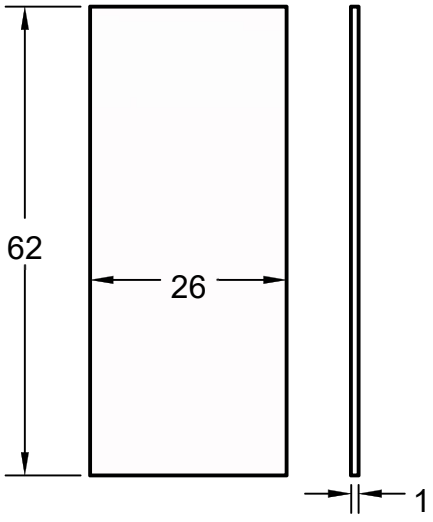

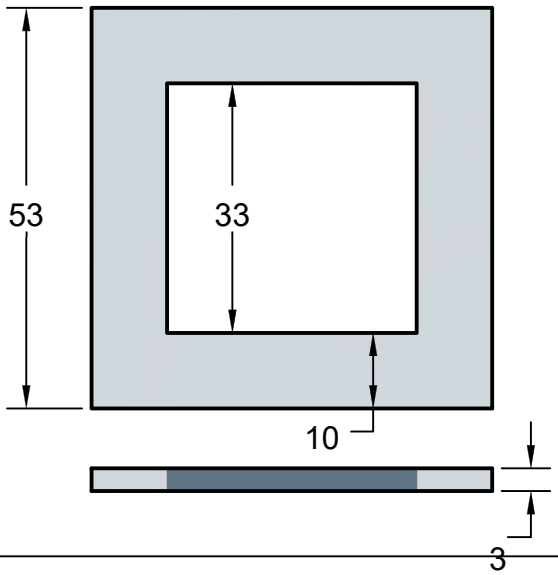

All units in millimeters

3mm depth of solvent corresponds to ~5mL

PROJECT

Sample Chamber

TITLE

Assembly

APPROVED	SIZE	CODE	DWG NO	REV
CHECKED	A			
DRAWN Alan Rohrbach 1/17/2019	SCALE 1:1	WEIGHT	SHEET 4/4	

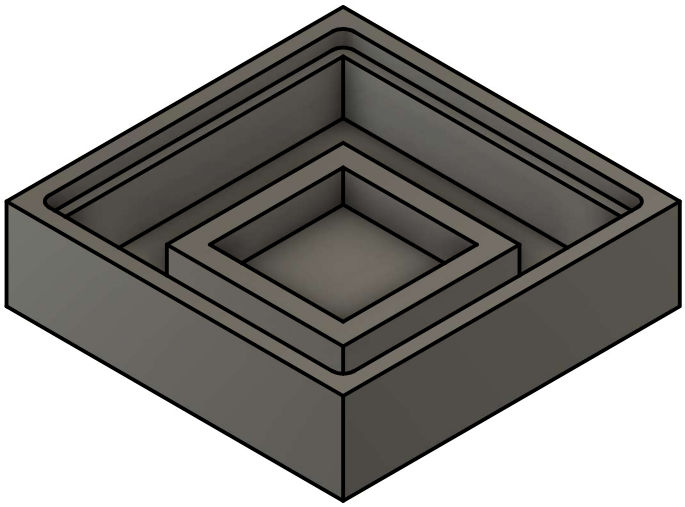

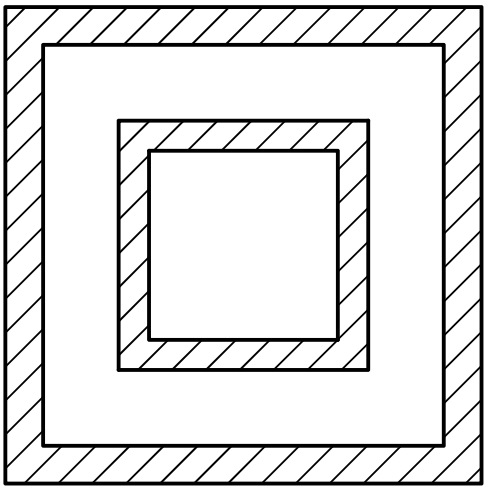

PROJECT

Sample Chamber

TITLE

Bottom

APPROVED	SIZE	CODE	DWG NO	REV
CHECKED	A			
DRAWN Alan Rohrbach 1/16/2019	SCALE 1:1	WEIGHT	SHEET 1/3	

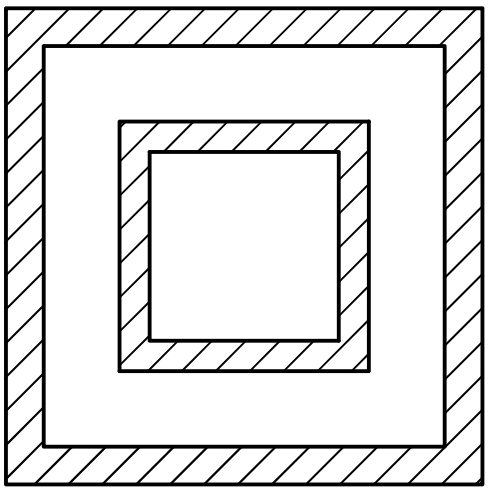

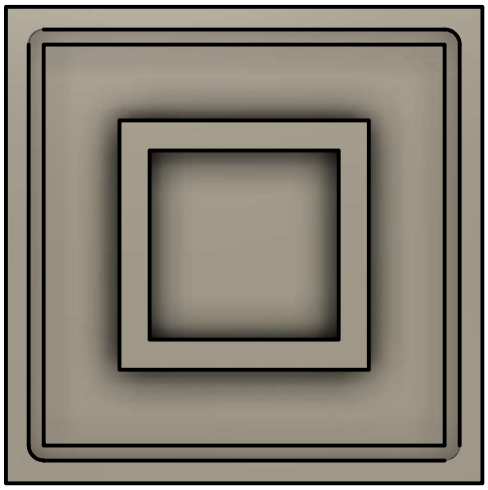

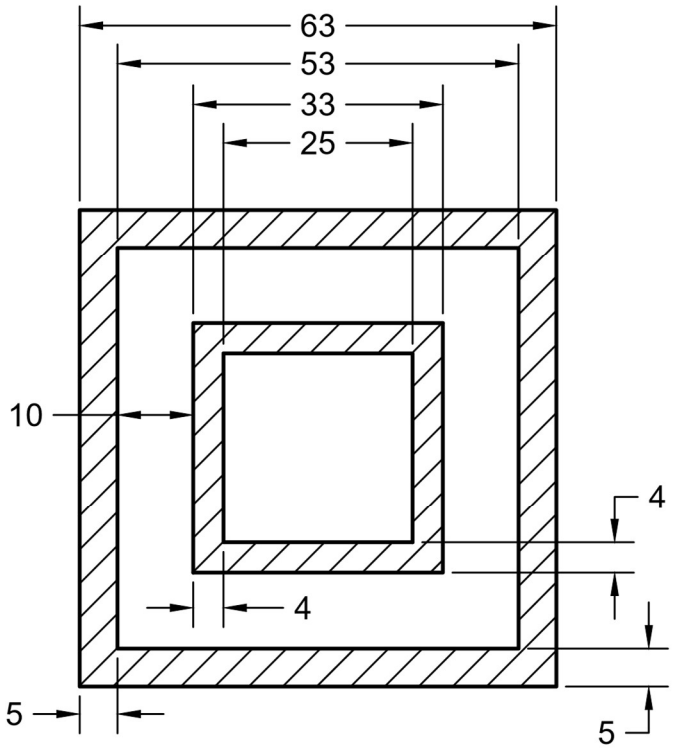

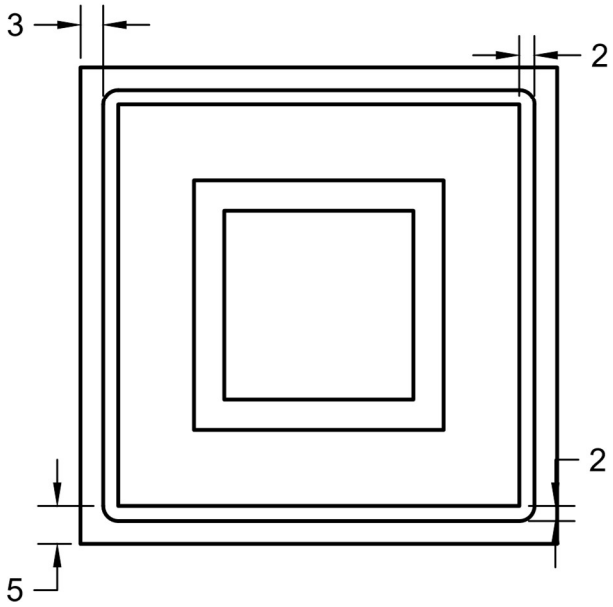

All units in millimeters

PROJECT

Sample Chamber

TITLE

Bottom

APPROVED	SIZE	CODE	DWG NO	REV
CHECKED	A			
DRAWN Alan Rohrbach 1/16/2019	SCALE 1:1	WEIGHT	SHEET 2/3	

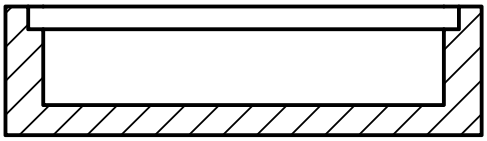

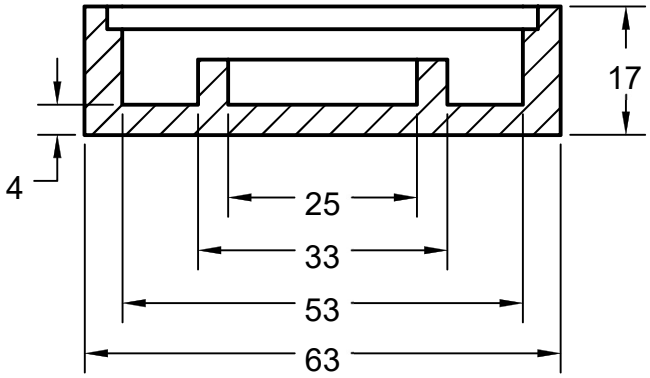

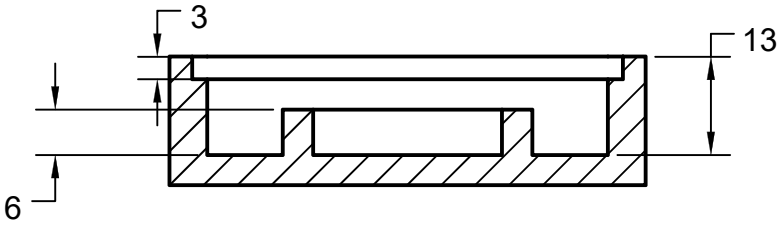

All units in millimeters

PROJECT

Sample Chamber

TITLE

Bottom

APPROVED	SIZE	CODE	DWG NO	REV
CHECKED	A			
DRAWN Alan Rohrbach 1/16/2019	SCALE 1:1	WEIGHT	SHEET 3/3	

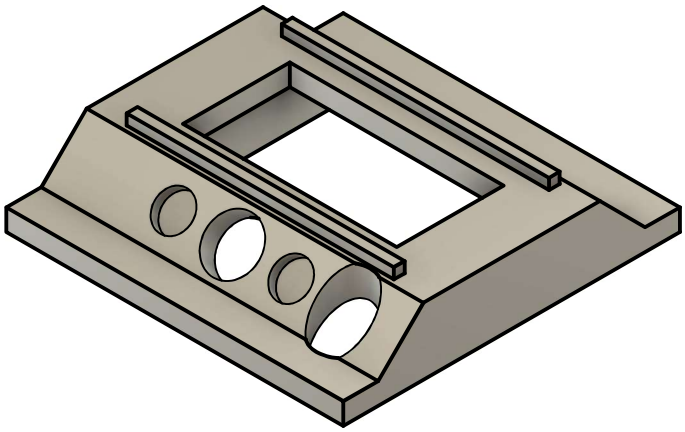

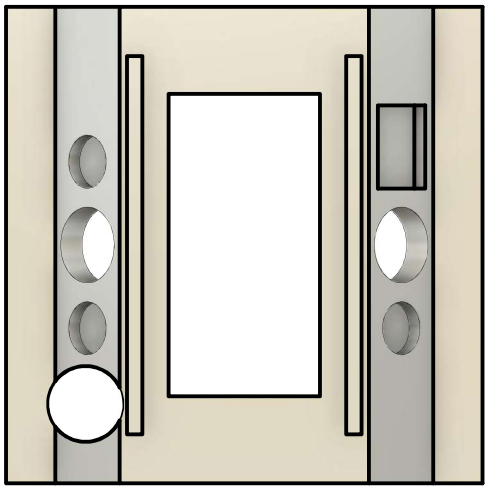

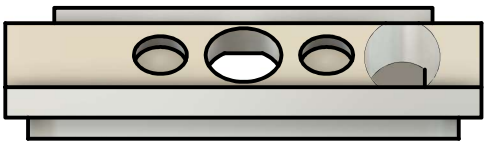

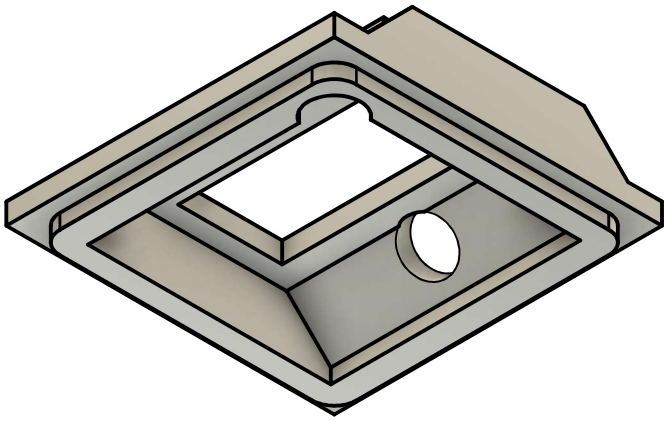

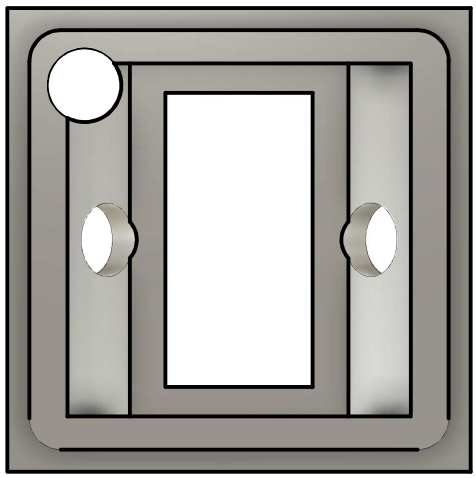

PROJECT

Sample Chamber

TITLE

Lid

APPROVED	SIZE	CODE	DWG NO	REV
CHECKED	A			
DRAWN Alan Rohrbach 1/17/2019	SCALE 1:1	WEIGHT	SHEET 1/3	

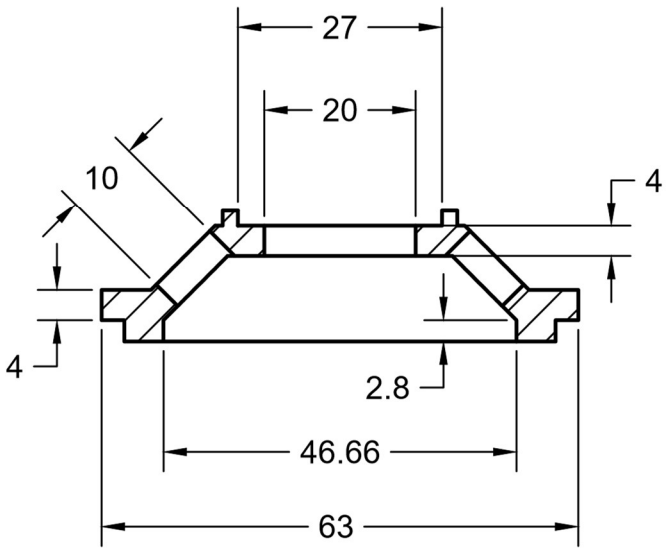

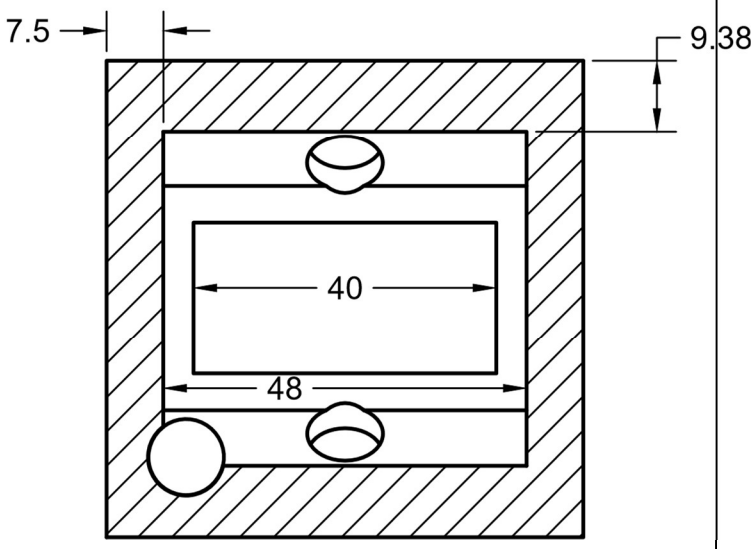

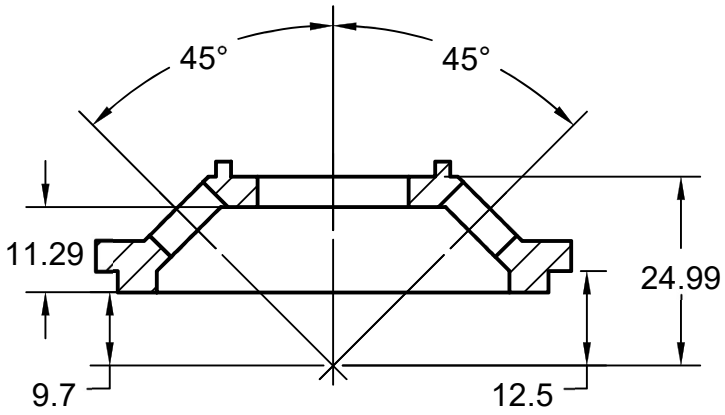

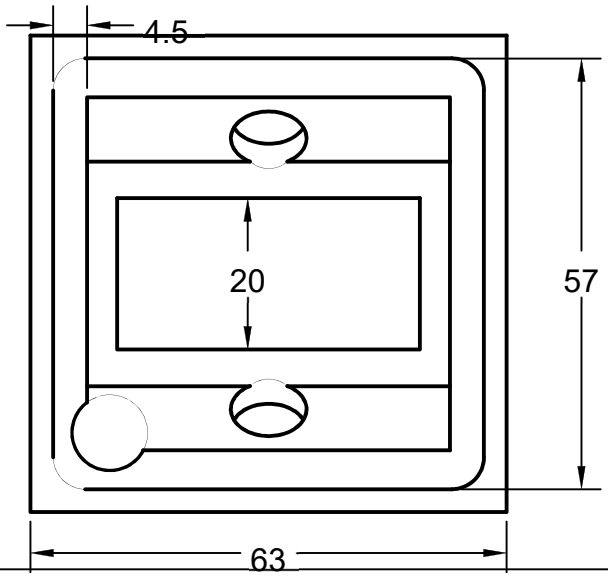

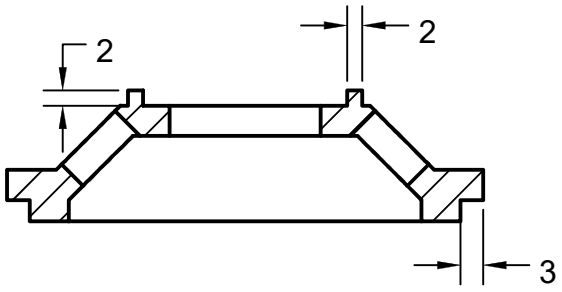

All units in millimeters

PROJECT

Sample Chamber

TITLE

Lid

APPROVED	SIZE	CODE	DWG NO	REV
CHECKED	A			
DRAWN Alan Rohrbach 1/17/2019	SCALE 1:1	WEIGHT	SHEET 2/3	

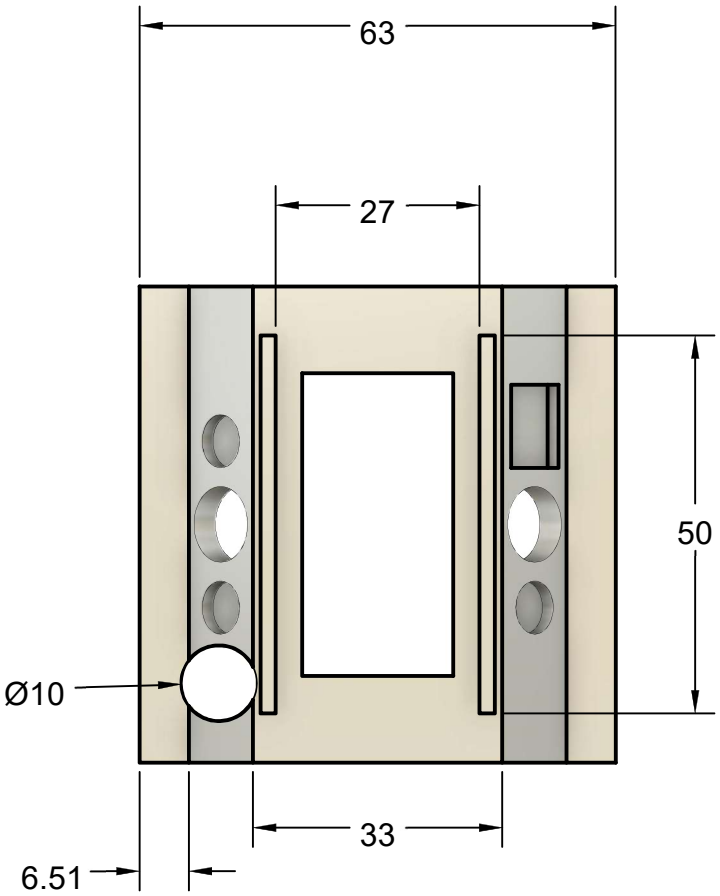

All units in millimeters

PROJECT
Sample Chamber

TITLE
Lid

APPROVED	SIZE	CODE	DWG NO	REV
CHECKED	A			
DRAWN Alan Rohrbach 1/17/2019	SCALE 1:1	WEIGHT	SHEET 3/3	